Atmos. Chem. Phys. Discuss., 11, 21713–21767, 2011
www.atmos-chem-phys-discuss.net/11/21713/2011/
doi:10.5194/acpd-11-21713-2011

Atmospheric Chemistry and Physics Discussions

Typical types and formation mechanisms of haze in an eastern Asia megacity, Shanghai

K. Huang[1,2], G. Zhuang[1], Y. Lin[1], J. S. Fu[2], Q. Wang[1], T. Liu[1], R. Zhang[1], Y. Jiang[1], and C. Deng[1]

[1]Center for Atmospheric Chemistry Study, Department of Environmental Science and Engineering, Fudan University, Shanghai, 200433, China
[2]Department of Civil and Environmental Engineering, The University of Tennessee, Knoxville, TN 37996, USA

Received: 13 July 2011 – Accepted: 21 July 2011 – Published: 2 August 2011

Correspondence to: G. Zhuang (gzhuang@fudan.edu.cn),
J. S. Fu (jsfu@utk.edu)

Published by Copernicus Publications on behalf of the European Geosciences Union.

Abstract

An intensive aerosol and gases campaign has been performed at Shanghai in the Yangtze River Delta region over Eastern China from late March to early June 2009. This study provided a complementary picture of typical haze types and formation mechanisms in megacities over China by using a synergy of ground-based monitoring, satellite observation and lidar inversion. During the whole study period, several extreme low visibility periods were observed with distinct characteristics, and three typical haze types were identified, i.e. secondary inorganic pollution, dust, and biomass burning. Sulfate, nitrate and ammonium accounted for a major part of $PM_{2.5}$ mass during the secondary inorganic pollution, and the good correlation between SO_2/NO_x/CO and $PM_{2.5}$ indicated that coal burning and vehicle emission were the major sources. Large-scale regions with high AOD and low Ångström exponent were detected by remote-sensing observation during the dust pollution episode, and this episode corresponded to coarse particles rich in mineral components such as Al and Ca with mineral aerosol contributing 76.8 % to TSP. The relatively low Ca/Al ratio of 0.75 combined with the air mass backward trajectory analysis suggested the dust source from Gobi Desert. Typical tracers for biomass burning from satellite observation (column CO and HCHO) and from ground measurement (CO, particulate K^+, OC, and EC) were greatly enhanced during the biomass burning pollution episode. The exclusive linear correlation between CO and $PM_{2.5}$ corroborated that organic aerosol dominated aerosol chemistry during biomass burning, and the high concentration and enrichment degree of arsenic (As) could be also partly derived from biomass burning. Aerosol optical profile observed by lidar demonstrated that aerosol was mainly constrained below the boundary layer and comprised of spheric aerosol (depolarization ratio <5 %) during the secondary inorganic and biomass burning episodes, while during the dust episode thick dust layer distributed at altitudes from near the ground to 1.4 km (average depolarization ratio = 0.122 ± 0.023) with dust accounting for 44–55 % of the total aerosol extinction coefficient. This study had illustrated a good picture of the typical haze types and proposed

ACPD
11, 21713–21767, 2011

that identification of the complicated emission sources was important for the air quality improvement in megacities in China.

1 Introduction

China is now undergoing tremendous challenges of air quality impairment due to rapid industrial and transportation expansion, sharply increased demands of fossil fuel usage and increasing populations. Primary pollutant concentrations grow as a power-law function of population, and in China large emissions were concentrated in the mega-city clusters, such as Jing-Jin-Ji (Beijing-Tianjin-Hebei), the Pearl River Delta and Yangtze River Delta (YRD) regions (Parrish and Zhu, 2009). The YRD region, on which this study was focusing, included the biggest city in China, Shanghai, and Jiangsu and Zhejiang provinces. It has a population of over 80 million people and occupied over 21 % of China's total gross domestic product (GDP).

Upon a globally decreasing trend of radiation, sunshine duration and sky visibility (Che et al., 2005; Kaiser and Qian, 2002; Wang et al., 2009), the YRD region had experienced substantially increasing haze days since 1990s (Chang et al., 2009; Che et al., 2007), which was attributed to the dimming effect of aerosol. Compared to Bejing and Guangzhou, the emissions of black carbon and NO_x in Shanghai were $2 \sim 3$ times higher ($2003 \sim 2005$) (Chan and Yao, 2008), and the emission of NO_x was predicted to increase 60–70 % by 2020 due to the expansion of transportation (Chen et al., 2006). Health effects, such as cardiorespiratory diseases and carcinogenesis were partially associated with air pollution (Kan et al., 2007; Ye et al., 2000; Zhao et al., 2003) and reductions of primary $PM_{2.5}$ from industrial sector and mobile sources showed good health benefits in YRD (Zhou et al., 2010). It was estimated that the total economic cost of health impacts due to particulate air pollution in urban areas of Shanghai in 2001 was approximately 625.40 million US dollars, accounting for 1.03 % of GDP of the city (Kan and Chen, 2004). In addition, the agriculture production was likely reduced by 2.5–9.2 % due to exposure to ambient ozone (Liu et al., 2009). Some air

ACPD
11, 21713–21767, 2011

quality research had been conducted in Shanghai and other areas in YRD. Investigation of major aerosol constituents were found to be sulfate, nitrate, ammonium (Wang et al., 2006; Yao et al., 2002; Ye et al., 2003) and organic aerosol (Feng et al., 2006; Feng et al., 2009; Yang et al., 2005a), concluding that fossil fuel combustion and vehicle emission were major sources of secondary components. Compared to Beijing, Shanghai had higher concentrations of black carbon (BC) and higher ratio of BC/CO, which were attributed to larger contribution from diesel burning (diesel powered vehicles and marine vessels) (Zhou et al., 2009). Ground based sunphotometer observation at various sites in YRD showed relatively high aerosol extinction to sunlight (AOD > 0.7) and high fraction of fine particles (Ångström exponent > 1.0) (Pan et al., 2010; Xia et al., 2007). Concentration and fraction of ultrafine (10–100 nm) particles in total particle counts at Taichang, YRD, were 2 ~ 3 times higher than those reported in the urban/suburban areas in North America and Europe (Gao et al., 2009). And one research on the background site Lin'an suggested that the aerosol properties were more close to urban areas rather than the suburban ones (Xu et al., 2002). Huang et al. (2008) found that there was a significantly decreasing trend of acid rain pH in Shanghai with 15-fold increased acidity during 1997–2005. However, the mechanism on the formation of haze was seldom discussed (Fu et al., 2008; Pathak et al., 2009; Zhou et al., 2009). Compared to some intensive field campaigns in the Pearl River Delta region and northeastern China, i.e. PRIDE-PRD2004, PRIDE-PRD2006 (Program of Regional Integrated Experiments on Air Quality over Pearl River Delta of China 2004 and 2006; Garland et al., 2008; Zhang et al., 2008), CAREBEIJING (Regional formation processes and controlling effects of air pollution before and during the Beijing Olympics: the results of CAREBEIJING; Wang et al., 2010), and EAST-AIRE (East Asian Studies of Tropospheric Aerosols: an International Regional Experiment; Li et al., 2007), no comprehensive initiatives have been carried out in YRD and especially, the source of haze, which was also referred to the atmospheric brown clouds (ABC), was not well disentangled due to the complicated aerosol sources in China currently.

ACPD
11, 21713–21767, 2011

In this study, an intensive field experiment using various techniques was targeted to determine the typical pollution types that caused the frequent occurrence of haze in Eastern China. Aerosol chemical and optical experiments were combined with remote-sensing observation to distinguish and characterize different types of haze. Comments and discussions were made to emphasize the importance of aerosol source determination, which were beneficial for the local governments to improve air quality and mitigate climate effects.

2 Methodology

2.1 Field observations

2.1.1 Automatic aerosol and gases monitoring

The Thermo Scientific TEOM 1405-D monitor simultaneously measured $PM_{2.5}$, PM-Coarse ($PM_{10-2.5}$) and PM_{10} mass concentration upon an oscillating balance. PM (particulate matter) accumulating on a filter mounted changes in the frequency of oscillation, which were related to the mass of material accumulating on the filter, were detected in quasi-real-time and converted by a microprocessor into an equivalent PM mass concentration every few seconds, as a 10 min running average. Sampler split a PM_{10} sample stream into its fine ($PM_{2.5}$) and coarse ($PM_{10-2.5}$) fractions using a USEPA-designed virtual impactor for the additional 2.5 µm cutpoint. The total flow rate operated at 16.67 l min^{-1}, and two separate flow controllers maintained the coarse particle stream at 1.67 l min^{-1} and the fine particle stream at 3.0 l min^{-1}. Besides, another Thermo Scientific TEOM 1405 monitor was set up to measure PM_1 mass concentration operating at 3.0 l min^{-1} with a bypass flow rate of 13.67 l min^{-1}. PM concentrations were averaged and used at intervals of 1hr in this study. Trace gases instruments included 43i SO_2 analyzer, 42i NO-NO_2-NO_x analyzer, 49i O_3 analyzer and 48i CO analyzer, zero and span checks were performed every week, all the data were also averaged at intervals of 1 h.

ACPD
11, 21713–21767, 2011

2.1.2 Manual sampling

Aerosol samples of TSP and $PM_{2.5}$ were collected on Whatman® 41 filters (Whatman Inc., Maidstone, UK) using medium-volume samplers manufactured by Beijing Geological Instrument-Dickel Co., Ltd. (model: TSP/PM_{10}/$PM_{2.5}$–2; flow rate: 77.59 l min^{-1}). Aerosol samples of PM_{10} were collected on Whatman quartz microfiber filters (QM/A, 18.5 cm × 23.7 cm) using the high-volume sampler (Thermo, flow rate: 1.00 m^3 min^{-1}). All the samplers were co-located with the online instruments on the roof (~30 m) of the 4th Teaching Building at Fudan University, Shanghai. The duration time of sampling was generally 24 h. More samples with shorter duration time were collected during the heavy haze days. The filters before and after sampling were weighed using an analytical balance (Model: Sartorius 2004MP) with a reading precision 10 mg after stabilizing in constant temperature (20 ± 1 °C) and humidity (40 ± 1 %). All the procedures were strictly quality controlled to avoid the possible contamination of samples.

2.1.3 Lidar observation

A dual-wavelength depolarization lidar (Model: L2S-SM II) developed by the National Institute for Environmental Studies (NIES) was operated in this field campaign. The lidar could measure backscattering coefficients and the depolarization ratio at wavelength of 532 nm. The Lidar employed a flash lamp pumped Nd:YAG laser with a second harmonics generator. The laser beam was vertically oriented to the sky after collimated with a beam expander. Transmitted laser energy was typically 20 mJ per pulse at 1064 nm and 30 mJ per pulse at 532 nm. The pulse repetition rate was 10 Hz. The scattered light was received with a 20 cm Schmidt Cassegrain type telescope collimated and directed to the dichroic mirror. The polarization components were detected with two photomultiplier tubes (PMTs). Detected signals were recorded with a transient recorder (digital oscilloscope), averaged and transferred to the data acquisition computer for the web interface. The lidar continuously operated with 15 min intervals and 30 m height resolution by setting a boundary condition at 3 km. The Fernald inversion

ACPD
11, 21713–21767, 2011

method (Fernald, 1984) was applied to deriving the extinction coefficient with lidar ratio (extinction-to-backscatter ratio) set to 50 sr (Liu et al., 2002) in inversion process.

2.2 Chemical analysis

2.2.1 Ion analysis

One-fourth of each sample and blank filter was extracted ultrasonically by 10 ml deionized water ($18M\Omega\,cm^{-1}$). Eleven inorganic ions (SO_4^{2-}, NO_3^-, F^-, Cl^-, NO_2^-, PO_4^{3-}, NH_4^+, Na^+, K^+, Ca^{2+}, Mg^{2+}) and four organic acids (formic, acetic, oxalic, and methylsulfonic acid (MSA)) were analyzed by Ion Chromatography (ICS 3000, Dionex), which consisted of a separation column (Dionex Ionpac AS 11), a guard column (Dionex Ionpac AG 11), a self-regenerating suppressed conductivity detector (Dionex Ionpac ED50) and a gradient pump (Dionex Ionpac GP50). The detail procedures were given elsewhere (Yuan et al., 2003).

2.2.2 Element analysis

Half of each sample and blank filter was digested at 170 °C for 4 h in high-pressure Teflon digestion vessel with 3ml concentrated HNO_3, 1 ml concentrated HCl, and 1ml concentrated HF. After cooling, the solutions were dried, and then diluted to 10 ml with distilled deionized water. Total 24 elements (Al, Fe, Mn, Mg, Mo, Ti, Sc, Na, Ba, Sr, Sb, Ca, Co, Ni, Cu, Ge, Pb, P, K, Zn, Cd, V, S, and As) were measured by using an inductively coupled plasma atomic emission spectroscopy (ICP-OES; SPECTRO, Germany). The detailed analytical procedures were given elsewhere (Sun et al., 2004; Zhuang et al., 2001).

2.2.3 Carbonaceous aerosol analysis

Quartz filters were pre-heated at 500° for 5 h before using and the samples were analyzed for OC/EC using DRI Model 2001 (Thermal/Optical Carbon Analyzer). The

ACPD
11, 21713–21767, 2011

IMPROVE thermal/optical reflectance (TOR) protocol (Chow and Watson, 2002) was used for the carbon analysis. The eight fractions (OC1, OC2, OC3, OC4 at 120, 250, 450 and 550 °C, respectively in a helium atmosphere, EC1, EC2, EC3 at 550, 700 and 800 °C, respectively, in the 98 % helium/2 % oxygen atmosphere) and OPC (optically detected pyrolized carbon) were measured separately. The IMPROVE protocol defined OC as OC1+ OC2+OC3+OC4+OPC and EC as EC1+EC2+EC3-OPC.

2.3 Satellite observation

In this study, a number of satellite sensors had been used to sense aerosol and trace gas information. The MODIS instrument (Moderate-resolution Imaging Spectroradiometer) provided a large regional view of aerosol distributions with a resolution of 10 × 10 km. Operational aerosol optical depths were reported at 0.55 μm by NASA (Chu et al., 2003; Kaufman et al., 1997). The total carbon monoxide column concentration retrieved from Atmospheric Infrared Sounder (AIRS) on board NASA's Aqua satellite were used to observe large scale transport from biomass burning sources (McMillan et al., 2005). Launched in 2004, the Dutch–Finnish built Ozone Monitoring Instrument (OMI) aboard NASA's EOS Aura satellite provided daily global coverage with a spatial resolution of 13 km × 24 km at nadir (Levelt et al., 2006), and the total formaldehyde column concentration had been used to study the signals of possible biomass burning source. Detailed description about the OMI instrument could be found elsewhere (Kurosu et al., 2004).

3 Results and discussion

3.1 Identification of three pollution episodes

An intensive aerosol characterization campaign was carried out in Shanghai over the Yangtze River Delta region in 2009, which aimed to get insights into the formation mechanisms of haze in Eastern China. The study period had a coverage of 30 March ~ 16 May and 28 May ~ 3 June, and the absent intervals between the two

ACPD
11, 21713–21767, 2011

time periods were due to malfunction and maintenance of some instruments. Haze was usually defined as an atmospheric phenomenon where dust, smoke and other pollutant particles reduced the visibility of the sky. Here we had calculated the visibility following the Koschmieder formula $L_V = 3.912/\sigma_{ext}$, where L_V was the visibility and the total extinction coefficient σ_{ext} was due to scattering and absorption by particles and gases. In order to compare with the recorded visibility data, we calculated the near-surface extinction coefficient caused by aerosol (σ_{ep}) by averaging the lidar measured aerosol extinction coefficient from the ground to an altitude of 300 m. Absorption of visible light by gases was considered to be essentially due to NO_2 and the absorption coefficient (σ_{ag}) could be estimated using the formula $\sigma_{ag} = 0.33 \times [NO_2]$ (Groblicki et al., 1981). Here, NO_2 was in units of $\times 10^{-9}$ V/V. Rayleigh scattering coefficient (σ_{sg}) was assumed to be a constant of 0.013 km^{-1} a.s.l. (Chan et al., 1999; Peundorf, 1957). The scattering coefficient of light due to moisture in the air (b_{sw}) could be neglected when relatively humidity (RH) was lower than 70 % (Cass, 1979; Chan et al., 1999). In this study, the average relative humidity was about 60 %. Consequently, the total light extinction by particles and gases ($\sigma_{ext} = \sigma_{ep} + \sigma_{ag} + \sigma_{sg}$) was calculated and the visibility could be estimated. Figure 1a shows the calculated hourly visibility and the recorded visibility at Pudong, which was about 32 km from the site in this study (An upper limit of $L_V = 10$ km was recorded at the meteorological station of Pudong). As shown in the figure, the visibility measured by two different approaches had relatively good time-series consistency, especially during the low visibility periods, which suggested that visibilities estimated from aerosol extinction profile and pollutant gas were reasonable and could be used for further analysis.

Figure 1b shows the temporal variation of PM mass concentration levels at three different sizes, i.e. PM_1, $PM_{2.5}$ and PM_{10}. Based on the visibility, PM mass concentration levels and mass fraction of fine particles ($PM_{2.5}/PM_{10}$), we had sorted out three typical pollution episodes. The first pollution episode (PE1) occurred from 4–10 April, during which the mean visibility was as low as 3.5 km. The average concentrations of PM_1, $PM_{2.5}$, and PM_{10} were 60.9 ± 14.0, 63.6 ± 16.4, and 120.1 ± 40.7 $\mu g\,m^{-3}$, respectively.

ACPD
11, 21713–21767, 2011

If we applied the US EPA 24-h standard of 35 $\mu g\,m^{-3}$, the fine particle concentration levels were much higher than this criteria. The average ratio of $PM_{2.5}/PM_{10}$ was 0.54 ± 0.09, indicating both fine and coarse particles could be important in the formation of pollution. The mass ratio of $PM_1/PM_{2.5}$ ranged from 0.90 to 0.99, indicating particles tended to accumulated in smaller sizes. Time series of pollutant gases, i.e. SO_2, NO_x and CO, showed their significant enhancements during this period (Fig. 2), enhanced industrial and traffic emissions were probably responsible for this and the pollution during this period was probably caused by the local photochemical process. The detailed analysis on pollutant gases would be discussed in Sect. 3.5. To study the aerosol transport characteristics, air mass backward trajectories were computed using the NOAA Hybrid Single-Particle Lagrangian Trajectory (HYSPLIT) model (R. Draxler and G. Rolph, HYSPLIT (HYbrid Single–Particle Lagrangian Integrated Trajectory) Model, 2003, http://www.arl.noaa.gov/ready/hysplit4.html) with meteorological data provided by the Global Data Assimilation System (GDAS). Three-day backward trajectories at the end point of Shanghai during PE1 showed that air masses flowed from various directions and traveled relatively short distances, reflecting the slow wind speeds. Additionally, the daily average mixing layer was almost below 500 m (Fig. 3a). This typical stagnant synoptic meteorological condition was especially unfavorable for the dispersion of particles and gases, and beneficial for the formation of haze pollution.

The second pollution episode (PE2) occurred on 25 April and lasted a short duration. The daily concentrations of PM_1, $PM_{2.5}$, and PM_{10} were 26.3, 53.0, and 174.5 $\mu g\,m^{-3}$, respectively. And the ratio of $PM_{2.5}/PM_{10}$ reached the lowest value of 0.35 over the whole study period, indicating the characteristic of coarse particle pollution. Combined with air backward trajectory analysis, we found that air masses starting at various altitudes of 500, 1000 and 3000 mall flowed from northern China, which passed over the Gobi Desert in Mongolia and Inner-Mongolia (Fig. 3b). The average wind speed reached as high as 7.5 $m\,s^{-1}$ in Shanghai with gust speeds over 10 $m\,s^{-1}$. Additionally, the intraday average mixing height was about 1000 m, much more elevated than PE1. Thus, all the evidences above indicated that this coarse particle pollution was

ACPD
11, 21713–21767, 2011

probably caused by the entrainment of dust aerosol from the desert in Mongolia and Inner-Mongolia via the long-range transport. Figure 4 depicts the regional distribution pattern of PM_{10} concentration during 24–26 April in northern and eastern China. On 24 April, high pollution ($PM_{10} > 300\,\mu g\,m^{-3}$) occurred in the northern China, mainly in Inner-Mongolia and Shanxi province while the eastern and southern China was virtually dust-free (Fig. 4a). On the next day, high level particles moved to major areas of central China and stretched to the eastern coastal regions (Fig. 4b). As for Shanghai, our monitoring station observed that the dust entrainment actually had the most significant impacts on local air quality during two periods, i.e. from 01:30 to 08:00 LST and 17:00 to 23:00 LST (Local Standard Time). The average PM_{10} concentration reached 258 and 236 $\mu g\,m^{-3}$, respectively, while the concentrations of fine particles and pollutant gases stayed at low levels (Figs. 1b and 2), which was due to the dilution effect of dust on local pollutants. Till 26 April, the PM levels in northern China had sharply declined and the dust continued to travel southwestward along the east coast, which exerted a moderate influence on air quality of southern China (Fig. 4c). In Shanghai, there was a significant decrease of PM_{10} concentration and an increase of $PM_{2.5}/PM_{10}$ ratio to over 0.50, indicating the re-dominance of fine particles after the pass of dust.

The third pollution episode (PE3) occurred from 28 May to 3 April. The average concentrations of PM_1, $PM_{2.5}$, and PM_{10} were 67.8 ± 37.6, 84.0 ± 48.4 and $135.6 \pm 71.4\,\mu g\,m^{-3}$, respectively, with the average $PM_{2.5}/PM_{10}$ratio of 0.65 ± 0.04. Fine particle concentration levels and its mass contribution to the total particles were both the highest among all three pollution episodes. Notwithstanding, the concentration levels of pollutant gases were not as high as PE1 except for CO, SO_2 was at a moderate level and NO_x was relatively low (Fig. 2). Opposite to the high concentrations of pollutant gases during PE1, the formation mechanism of the PE3 pollution should be different from that of PE1. The meteorological conditions during this period were as similar as PE1, i.e. slow transport of air masses and relatively low mixing layer as shown in Fig. 3c, which also suggested the stagnant atmospheric condition during PE3.

ACPD
11, 21713–21767, 2011

However, it was still difficult to identify the pollution types of different episodes based on the limited information such as PM, pollutant gases and meteorological parameters. In the discussions below, we will demonstrate more evidences from the aerosol optical and chemical properties.

3.2 Regional characteristics and possible sources via remote sensing observation

The remote sensing analysis from satellite observation is a good way to indicate the spatial distribution, transport and possible source of airborne pollutants. Figure 5 shows the observed satellite signals during the three episodes, respectively. During PE1, zones of high aerosol optical depths (AOD) at the wavelength of 550 nm retrieved from MODIS were mainly concentrated in Jing-Jin-Ji (Beijing-Tianjin-Hebei), Shandong, Anhui, Henan, Hubei provinves, and the Yangtze River Delta region, including northern part of Zhejiang, Jiangsu provinces and Shanghai (Fig. 5a). The average AOD value over Shanghai reached extremely high value of over 1.2, indicating strong aerosol extinction to sunlight in the atmosphere. Figure 5b shows the spatial distribution of Ångström exponent at the wavelength range from 470 to 670 nm. Ångström exponent was a good indicator of the aerosol size distribution, the larger this parameter, the smaller the particle size, and vice versa. The spatial pattern of Ångström exponent didn't resemble that of AOD. In some regions that the AOD values were moderate such as southern parts of Zhejiang province and major parts of central China, the Ångström exponents ranged from 1.3 to 1.5, indicating these regions were mainly dominated by fine particles. While in the high AOD regions that discussed above, the Ångström exponents were not correspondingly high and ranged from 0.8 to 1.2, which suggested there was non-negligible contribution of coarse particles during PE1. This was consistent with the moderate $PM_{2.5}/PM_{10}$ ratio that measured by our ground monitoring as discussed in Sect. 3.1. As shown in Fig. 5b, there was a belt of relatively low Ångström exponent extending from the Bohai Bay and the Shandong Peninsular to the Yangtze

ACPD
11, 21713–21767, 2011

River Delta region along the east coast. The continuity of Ångström exponent probably indicated that the Yangtze River Delta could have been more or less influenced from the northern China. As PE1 was in the spring season when the occurrence of floating dust was frequent and ubiquitous, the downstream regions were probably influenced by the transport of dust aerosol to some extent.

During PE2, high AOD values were observed in most parts of the study domain, which was as similar as PE1 to a certain extent, especially in the central and eastern parts of China with AOD exceeding 1.2 (Fig. 5c). Anyway, Ångström exponents were much lower than PE1. It ranged from 0.5 to 0.6 (Fig. 5d), indicating considerable existence of coarse particles, which was consistent with ground measurements. And there were almost no regional gradients of the Ångström exponents, suggesting this episode was characteristic of large-scale influences. In Sect. 3.1, we have proposed that this pollution episode should be impacted by the invaded dust, and it was confirmed here by using the remote sensing analysis.

During PE3, large quantities of fire spots retrieved from MODIS were observed in the study domain (denoted by black dots in Fig. 5e–g), and they were mainly located in the conjunction of western Shanghai and southern Jiangsu province, major parts of Jiangsu, northern Zhejiang, northern Anhui province and eastern parts of Shandong province. The total column concentration of carbon monoxide (CO) retrieved from the Atmospheric Infrared Sounder (AIRS) showed very good spatial pattern with that of fire spots (Fig. 5e). In the normal times, the major sources of CO were derived from anthropogenic sources, such as traffic and/or industrial emission. While it was a major product emitted from biomass burning along with many trace gases such as carbon dioxide (CO_2), methane (CH_4), nitrous oxides (NO_x) and hydrocarbons (Crutzen and Andreae, 1990). Various studies had used CO as tracer for biomass burning in aircraft measurement (Boian and Kirchhoff, 2004), satellite observation (Choi and Chang, 2006; Mari et al., 2008) and other measurements (Kato et al., 1999; Kato et al., 2002). The column concentration of CO over the intense burning areas reached 2.5 $\sim 3.0 \times 10^{18}$ molecules cm^{-2} as shown in the figure, evidently distinguished from

ACPD
11, 21713–21767, 2011

areas free of biomass burning and close to the levels when biomass burning occurred in northeastern China (Choi and Chang, 2006). Besides, the Ozone Monitoring Instrument (OMI) also detected high formaldehyde (HCHO) columns over the intense burning areas (Fig. 5f). HCHO was a primary emission product from biomass burning, which was an intermediate product from the oxidation of hydrocarbons. And it was a good indicator of the local photochemical source as it only had a lifetime of a few hours. HCHO columns over the hotspot regions were greater than 3.0×10^{16} molecules cm^{-2}, more than a factor of 2–4 larger than the areas free of fires. Significant correlation between HCHO columns and fire counts had ever been observed (Marbach et al., 2008; Palmer et al., 2007). Thus, the enhancement of CO and HCHO in the accumulated fire spot regions indicated that the pollution during PE3 should be caused by biomass burning. The biomass emission resulted in high AOD values where large fire spots occurred, with the highest AOD up to about 2.0 in the Yangtze River Delta region. However, compared to the spatial distribution of CO and HCHO, the high AOD levels didn't always coincide with the fire regions. For example, there was no fire spots observed in Jiangxi province with low CO concentrations, but a high AOD region was found there. While as for Shandong province, the regions with great fire spots, high CO, and HCHO concentrations were at the relatively low AOD level. This suggested that CO and HCHO were more sensitive to biomass burning than AOD as AOD represented the overall extinction of various emission sources to light rather than the single source from biomass burning. The relatively low AOD over the Shandong Peninsula could have been due to the cleanup effect of the sea breezes as it was close to the sea. Anyway, the relatively good consistency between the observed satellite signals (e.g. carbon monoxide, formaldehyde and aerosol optical depth) over Eastern China and the fire hotspots clearly indicated that biomass burning should be the major cause of heavy haze during this period. Every year during May, June and October in Eastern China, crop residues after harvest were either directly returned to agriculture fields as fertilizer, burned in the field, or used as biofuels. It has been previously reported that biomass burning usually occurred during the transition period from spring to summer

ACPD
11, 21713–21767, 2011

(Wang et al., 2002) and in autumn (Xu et al., 2002), which was due to the burning of post-harvest straws by human activities.

In this section, the remote sensing analysis had given us some highlights into the different characteristics of three pollution episodes, including possible sources and transport pathways and provided some consistent results to our ground measurements. However, there were large uncertainties due to satellite detection limit of the small fire size of the field crop residue burning that could be possibly missed by satellite observations (Chang and Song, 2010; Yan et al., 2006). And satellites could not capture all fire events occurring during this study period, because fires hidden under clouds could not be easily detected. Additionally, satellite overpass also brings about the missed detection of hotspots.

3.3 Aerosol chemistry under different atmospheric conditions

In order to further identify the different types of hazes as envisioned by the discussion above, we have demonstrated the results of aerosol chemical measurements here. Figure 6 shows the temporal variations of some typical aerosol components during the whole study period. Time series of three major secondary inorganic species in $PM_{2.5}$, i.e. SO_4^{2-}, NO_3^-, and NH_4^+ were presented in Fig. 6a. Obviously, the total concentrations of the three species above exhibited the highest levels during PE1 with average concentrations of $48.86 \pm 5.01\,\mu g\,m^{-3}$, which accounted an average of 77 % to $PM_{2.5}$ mass. As precursors of sulfate and nitrate, SO_2 and NO_x also showed the highest levels during this episode which had been stated in Sect. 3.1. This suggested that the pollution during PE1 was dominated by the secondary inorganic aerosol. In addition, we found that during EP3, these species also exhibited a moderate concentration level with average values of $27.12 \pm 7.37\,\mu g\,m^{-3}$, which probably indicated that biomass burning could also released considerable amounts of inorganic pollutants. For the other periods, the levels of theses species were much lower with values almost below $20\,\mu g\,m^{-3}$. The average sulfate level during the whole study period was $8.0 \pm 5.8\,\mu g\,m^{-3}$. Compared to the previous studies (Fu et al., 2008; Pathak et al., 2009; Wang et al., 2006;

ACPD
11, 21713–21767, 2011

Yao et al., 2002; Ye et al., 2003), sulfate was much lower in this study, indicating the effective policy controls on the SO_2 emission. However, the average nitrate concentration reached $6.3 \pm 5.7\,\mu g\,m^{-3}$, comparable or even higher than those previous results. Additionally, the mass ratio of NO_3^-/SO_4^{2-} of 0.75 ± 0.26 in this study had an increasing trend as compared to the values of 0.64 in 2006 (Wang et al., 2006), and 0.43 during 1999–2000 (Yao et al., 2002; Ye et al., 2003). The ratio of NO_3^-/SO_4^{2-} could be used as an indicator of the relative importance of stationary vs. mobile sources (Arimoto et al., 1996) and the results indicated that the role of mobile emission had become more and more significant due to the rapid expansion of transportation.

Figure 6b shows the temporal variation of elemental Al concentration, the ratio of Ca/Al, and the estimated mass fraction of mineral aerosol in the total suspended particles (TSP). Al was one of the inert and abundant elements in mineral aerosol and had been used as a good tracer for mineral aerosol in various studies (Huang et al., 2010; Wang et al., 2007; Zhang et al., 2010). As shown in the figure, the highest Al concentration occurred on 25 April, i.e, the second pollution episode (PE2). The daily Al concentration reached as high as $13.7\,\mu g\,m^{-3}$, almost $2 \sim 3$ times that of the other periods. To quantify the mass concentration of mineral aerosol, it could be estimated by summing the major mineral elements with oxygen for their normal oxides, which was calculated using the formula: [Mineral concentration] = 2.2[Al] + 2.49[Si] + 1.63[Ca] + 2.42[Fe] + 1.94[Ti] (Malm et al., 1994). According to this estimation, the percentage of mineral aerosol in TSP during PE2 was as high as 76.8 %. Oppositely, the average concentration of sum of SO_4^{2-}, NO_3^-, and NH_4^+ in $PM_{2.5}$ was only $11.23 \pm 5.25\,\mu g\,m^{-3}$, which was the lowest during the whole study period, indicating the dominance of non-anthropogenic sources and the prominent impact of dust entrainment on the local aerosol chemistry. To further characterize the origin of dust, the temporal variation of the elemental Ca/Al ratio was investigated as different dust regions in China were characterized of distinct Ca content and Ca/Al ratios in soils/particles (Zhang et al., 2003; Zhang et al., 1996). The Ca/Al ratio during PE3 reached a low value of 0.75, while in the other period it mainly ranged between 1.0 and 2.0. The

ACPD
11, 21713–21767, 2011

relatively high Ca/Al ratios during the non-dust periods were attributed to the frequent construction activities in recent years in Shanghai (Wang et al., 2006). The significant drop of Ca/Al ratio during PE2 confirmed that the local air quality must have been impacted by the outside sources. Elemental ratios of Ca/Al of dust aerosol in the three major dust source regions of China, i.,e., Gobi Desert, Loess Plateau, and Taklimakan Desert, were 0.52 ± 0.05, 1.09 ± 0.13, and 1.56 ± 0.14, respectively (Huang et al., 2010). Combined with the backward trajectory analysis in Sect. 3.1, we could confirm that the aerosol chemistry over Shanghai during PE2 was more close to that of the dust aerosol originating from Gobi Desert.

Figure 6c shows the temporal variation of particulate K^+ concentration in $PM_{2.5}$, which was a good indicator for tracing the biomass burning source (Andreae, 1983). Its highest level occurred just during PE3, with the average concentration of $2.84\,\mu g\,m^{-3}$, elevated $5 \sim 10$ times compared to the other days. As K^+ could be also derived from soil and dust, we used the K/Fe ratio of 0.56 (Yang et al., 2005b) to exclude the contribution of mineral source. It was calculated that the biomass burning derived K^+ could contribute about 80 % of total K^+, indicating the significant influence of biomass burning. The total potassium accounted for an average of 3.25 % in $PM_{2.5}$, also higher than that of 1.07 % in the other times and close to that of 3.58 % observed during the Mount Tai Experiment 2006 (MTX2006) which focused on biomass burning in Eastern China (Deng et al., 2011). Cl^- and K^+ were both important ions in particles from open burning of agricultural wastes (Li et al., 2007a). In this study, a very high correlation between Cl^- and K^+ was observed with the correlation coefficient of 0.96. Individual particle analysis also found that large irregular shaped KCl particles existed in young smoke (Chakrabarty et al., 2006; Li et al., 2003). Another significantly enhanced group of aerosol was the organic aerosol, including organic carbon (OC) and element carbon (EC). OC and EC in PM_{10} averaged 35.8 ± 8.1 and $5.7 \pm 1.3\,\mu g\,m^{-3}$ during PE3, and they were enhanced 30–100 % compared to the other days. The concentration level of organic aerosol was comparable to the extensive burning biomass period during MTX2006 (EC: $7\,\mu g\,m^{-3}$, OC: $24\,\mu g\,m^{-3}$) (Yamaji et al., 2010). If we

ACPD
11, 21713–21767, 2011

applied an OM/OC ratio of 1.8 to estimate the mass of organic matter (OM) (Turpin and Lim, 2001), the average mass contribution of OM to PM_{10} would be as high as 50 %. However, a higher factor (2.2–2.6) for aerosol heavily impacted by smoke was recommended (Turpin and Lim, 2001), thus it may result in an underestimated value for the faction of OM in this work. Compared to previous results of the mass percentage of organic aerosol of ∼30 % over YRD in the non-biomass-burning times (Feng et al., 2009; Yang et al., 2005a), biomass burning evidently emitted much more hydrocarbons. The OC/EC ratio was commonly on the order of 3 in most urban cities of China (Zhang et al., 2008), where the major sources of OC and EC were dominated by fossil fuel combustions. High ratio of OC/EC (6.4) was observed during PE3, which indicated that biomass burning contributed far more organic carbon than fossil fuel combustion did (Yan et al., 2006). Field measurements also observed a high ratio of OC/EC (5) for the burning of wheat straw and an even higher ratio for maize stover (Li et al., 2007).

Figure 7 shows the enrichment factors (EF) of major elements in $PM_{2.5}$ during three episodes, respectively, which aimed to evaluate the enrichment extents of various elements in aerosol. Usually Al was used as the reference element as it was a relatively chemical inert element and almost had no anthropogenic sources. The calculation formula was $EF_x = (X/Al)_{aerosol}/(X/Al)_{crust}$, of which X was the element of interest. Species with EFs less than 10 were usually considered to have a major natural source, which included Sc, Na, Ca, Co, Fe, Mn, Sr, Ba, P, K, Ni, Mn, Ti, and V. While species with higher EFs were contaminated by anthropogenic sources, which included Cu, Mo, As, Sb, Ge, Pb, Zn, Cd, S, and Se. As shown in the figure, the enrichment degrees of almost all the elements were the lowest during PE2. The dust aerosol originating from the Gobi Desert was relatively clean (Huang et al., 2010), and its entrainment had a cleanup and dilution effect on the local pollution, which lowered the enrichment degrees of most pollution elements. Elements during PE1 were mostly enriched, especially for those elements, i.e, Pb, Zn, Cd, S, and Se, with EF values larger than 1000. Pb had the major source from traffic emission in early years, while coal combustion had dominated the lead pollution after the phasing out of leaded gasoline in

ACPD
11, 21713–21767, 2011

1997 in Shanghai (Chen et al., 2005; Tan et al., 2006; Zhang et al., 2009). Zn and Cd mainly derived from local industrial and traffic emission (Cao et al., 2008; Shi et al., 2008). As indicators for coal combustion (Nriagu, 1989), S and Se had the highest EFs among all the elements, indicating coal combustion was one of the major sources of air pollution in Shanghai. Most of the EFs of pollution elements during the biomass burning period, i.e. PE3, were higher than PE2 and lower than PE1. The only exception was arsenic (As), whose EF was comparable to that during PE1. The average As concentration during PE3 was 7.53 ng m^{-3}, higher than that of 4.46 ng m^{-3} during PE1 and much higher than 2.02 ng m^{-3} in the normal periods. The high concentration and great enrichment of As should not be derived from its usual source such as coal burning, as no corresponding enrichment of the other pollution elements were found as in the PE1 case. High arsenic levels in groundwater in many areas over mainland China were observed (Mandal and Suzuki, 2002) and crop was most susceptible to As toxicity which sourced from the As-contaminated groundwater used for irrigation (Brammer and Ravenscroft, 2009). Thereby, the burning of agricultural residues would probably release considerable amounts of As, which resulted in the enrichment of As in particles.

3.4 Aerosol vertical profile

Figure 8 shows the time-height cross-section of the lidar measured aerosol properties at the wavelength of 532 nm during the three pollution periods, respectively. In this study, the total aerosol extinction coefficient was split to non-dust (spherical aerosols such as air pollution) and dust (nonspherical aerosol) fractions based on the aerosol depolarization ratio. Sugimoto et al. (2002) and Shimizu et al. (2004) described details of lidar observation and splitting method. Figure 8a presents the time-height cross-section of spheric aerosol extinction coefficient during PE1. Lidar observation successfully captured several high extinction peaks, which was consistent with the ground observation (Fig. 1b). Vertical distribution of aerosol extinction coefficient exhibited strong variations and showed obvious decreasing gradients from the ground to upper

ACPD
11, 21713–21767, 2011

layers, which reflected that pollutants were mainly constrained near the surface ground. The height of the boundary layer could be visually assumed from the vertical profile of aerosol optical properties. The profile, where the extinction coefficient sharply decreased, could be determined as the top of planetary boundary layer (PBL) (Noh et al., 2007). During the daytime, the PBL height was relatively high, and sometimes it could reach up to 2 km, which was due to the higher temperature and strong air convection. While during nighttime, it dropped to less than 0.5 km due to the temperature inversion. We selected one typical day (6 April) during PE1 to discuss its vertical profile (Fig. 9a). The depolarization ratio at the wavelength of 532 nm (δ_{532}) from the ground to the upper layer (~1.5 km) was less than 5 %, indicating the aerosol was mainly composed of spheric particles. While at higher altitudes, the depolarization ratio increased a little bit, which could be due to the absence of spheric aerosol or the possible contamination of water clouds and ice clouds. The averaged profile of attenuated aerosol backscattering coefficient showed a steep decreased gradient from 0.037 km^{-1} sr^{-1} near the ground to 0.0018–0.0030 km^{-1} sr^{-1} around 1–1.5 km.

As for PE2, we presented the time-height cross section of depolarization ratio during 22–28 April (Fig. 8b). The depolarization ratio showed high values on 25 April. The high depolarization ratio of aerosol was due to the nonsphericity (irregular shapes) and relatively large size of particles (Mcneil and Carswell, 1975) and we regarded this type of aerosol as mineral aerosol/dust aerosol for that dust was the most important component of nonspheric aerosols in East Asia. On 25 April, two consecutive dust plumes were observed, which was consistent with the ground measurement. We selected one dust plume (01:30–08:00 LST, 25 April) to discuss its vertical profile (Fig. 9b). In addition to the profile of aerosol backscattering coefficient and total depolarization ratio, the fraction of dust aerosol extinction to the total aerosol extinction (f_d) was also calculated based on the splitting method described by (Shimizu et al., 2004; Sugimoto et al., 2002). Compared to PE1, and PE3 that would be discussed below, PE2 showed evidently different profile. The backscattering coefficient sharply decreased from 0.04 km^{-1} sr^{-1} near the surface to 0.01 km^{-1} sr^{-1} at around 0.7 km. And then

ACPD
11, 21713–21767, 2011

the coefficient almost stayed constant value of about 0.01 km^{-1} sr^{-1} between 0.7 and 1.0 km, which indicated the transport of outside aerosol and this phenomena hadn't been observed in the other two episodes. Upwards, the backscattering coefficient started to sharply decrease again to low values. This type of vertical distribution of backscattering coefficient was closely related to the profile of depolarization ratio. As shown in the figure, there was an increase of δ_{532} from ground and peaked at around 1.0 km with value of 0.155. Correspondingly, the contribution of dust aerosol extinction to the total aerosol extinction peaked between 0.7 and 1.0 km with the values ranging from 51 % to 57 %. Thus, the relatively constant backscattering coefficient between altitudes of 0.7 and 1.0 km should be due to the increase of dust aerosol. Above this layer, f_d was less than 10 %, indicating the negligible existence of nonspheric aerosol in the upper layers. Using a threshold of δ_{532} = 0.06 to distinguish dust from other types of aerosol (Liu et al., 2008), the dust layer mainly distributed between ground and up to an altitude of around 1.4 km. The average δ_{532} value of this layer was 0.122 ± 0.023, which was close to the dust observed in Korea that sourced from the same dust region (Kim et al., 2010). Above this layer, the δ_{532} values decreased to low values, indicating the transport of dust at relatively low altitudes. Actually, most of the dust plumes (approximately 70 %) were observed near the ground (Kim et al., 2010). The contribution of dust aerosol extinction to the total aerosol extinction exhibited high values and relatively small vertical variations from near the ground to the upper layer of around 1 km, ranging from 44 % to 55 %. If we applied the dust and soluble aerosol extinction efficiency (σ_{ep}) of about 0.5 and 3 m^2 g^{-1}, respectively (Lee et al., 2009), it could be estimated that the mass concentration of dust aerosol was almost 4~7 times that of spheric aerosol by using the formula, $\sigma_{ep} = \beta_{ext}/M$, of which β_{ext} and M represented the extinction coefficient and mass concentration of dust/spheric aerosol. This was consistent with our ground measurement that dust aerosol contributed 76.8 % to the total aerosol mass as discussed in Sect. 3.3.

Figure 8c shows the time-height cross-section of spheric aerosol extinction coefficient during PE3. As similar as PE1, high aerosol extinction coefficients and strong

ACPD
11, 21713–21767, 2011

temporal variations were observed. Compared to PE3, the PBL height during this period was even lower. Figure 9c shows the vertical profile of backscattering coefficient and depolarization ratio on 1 June. The depolarization ratio fluctuated within 0.05 in the whole layer, indicating the dominance of spheric particles. The backscattering coefficient was about 0.024 $km^{-1}\,sr^{-1}$ near the surface, much lower than PE1 and PE2. While the fine aerosol concentration during PE3 was the highest. The non-linearity between PM concentrations and optical properties should be due to the different chemical compositions among different periods. In biomass burning, organic aerosol dominated while sulfate ammonium, nitrate ammonium dominated during the secondary inorganic pollution episode. The mass scattering efficiency ($m^2\,g^{-1}$) of organics was about a factor of $2 \sim 3$ lower than that of sulfate (Hasan and Dzubay, 1983; Ouimette and Flagan, 1982), thus this discrepancy resulted in the non-linearity between PM concentrations and optical properties.

3.5 Trace gases

Figure 10 compares the concentrations of trace gases among three pollution episodes and the normal period. The normal period was defined as the remaining days excluding the three pollution episodes. O_3 during PE1 was the lowest with average concentration of $79 \pm 63\,\mu g\,m^{-3}$, and O_3 and NO_x were strongly anti-correlated, which was due to the titration effect of nitrogen oxides as the Yangtze River Delta was under a strong VOC-limited regime (Geng et al., 2009). O_3 was highest during PE3 with average concentration of $96 \pm 63\,\mu g\,m^{-3}$, which could be caused by the relatively high emission of hydrocarbons emitted from biomass burning and the relatively weak titration effect due to NO_x. During PE1, the average concentrations of SO_2, NO_x and CO reached 54, 150, and $1334\,\mu g\,m^{-3}$, respectively. Compared to the heaviest pollution recorded at Shanghai on 19 January in 2007, when the daily concentration of SO_2 and NO_2 reached 194 and $123\,\mu g\,m^{-3}$, respectively (Fu et al., 2008), the concentration of SO_2 in this study was obviously lower, which could be due to the energy

ACPD
11, 21713–21767, 2011

policies in China that mitigated the SO_2 emission, including desulfurization of coal-fired power plant plumes, decommissioning of coal-fired boilers in manufacturing facilities and small power plants, conversion of domestic coal use to cleaner fuels and etc. (Fang et al., 2009). The emission of SO_2 almost remained constant during 1996–2005 (Chan and Yao, 2008) and energy policy scenarios claimed that SO_2 emissions during 2000–2020 would maintain the same level as in 2000 (Chen et al., 2006). The problem for the present and future would be nitrogen oxides. The average concentration of NO_2 and NO_x during PE1 reached high levels of 109 and 150 $\mu g\,m^{-3}$, respectively. Even during the normal period, their concentration was 60 and 99 $\mu g\,m^{-3}$, respectively, contrasting to 3–40 ppbv NO_x (1ppbv NO_x equaled to about 1.9 $\mu g\,m^{-3}$) in 2007 (Geng et al., 2009) and 5–35 $\mu g\,m^{-3}$ NO_x in 1999 (Wang et al., 2003). Satellite observation and model simulation both detected and predicted a strong increase of NO_2 in Eastern China, especially after 2000 (He et al., 2007), and Shanghai had a significantly linear increase of NO_2 column concentrations with about 20 % per year during the period of 1996–2005 (van der A et al., 2006), which was the rapidest among all the megacities in China (Zhang et al., 2007). Due to the expansion of transportation system, NO_x emissions were projected to increase by 60–70 % by 2020 (Chen et al., 2006). Therefore, it could explain the relatively high concentration of particulate nitrate and increasing ratio of SO_4^{2-}/NO_3^- as discussed in Sect. 3.3. Correspondingly, the effect of enormous vehicle emission had also been reflected in the carbon monoxide level. A significant correlation between CO and NO_x during PE1 was observed with the correlation coefficient of 0.86, indicating their common sources. Average concentration of CO during PE1 reached $1334 \pm 884\,\mu g\,m^{-3}$, greatly enhanced as compared to the normal period of $884 \pm 267\,\mu g\,m^{-3}$, 500–900 $\mu g\,m^{-3}$ in 1999 (Wang et al., 2003) and 654 ppbv (1 ppbv CO equaled to about 1.2 $\mu g\,m^{-3}$) in 2005 (Zhou et al., 2009). Due to increases of vehicle population and mileages in China, the emissions of NO_x and CO that apportioned to vehicular emission inventory had increased at an annual rate of 15 % and 14 % from 1980 to 2005, respectively. Especially, the Yangtze River Delta, which covered only 2.2 % of the total territory of China, generated about 19 % of total

ACPD
11, 21713–21767, 2011

vehicular pollutants in 2005 (Cai and Xie, 2007).

During the biomass burning period, the concentration levels of SO_2 and NO_x were much lower than during PE1 and close to the normal period. While CO was considerably enhanced with the average concentration of 1241 ± 352 $\mu g\,m^{-3}$, which was close to PE1 and much higher than the other periods. This probably suggested that biomass burning could release large amounts of CO while contributed little to the SO_2 and NO_x emission. Laboratory and field measurements of several types of crops in eastern China showed that the emission factor of SO_2 (0.44–0.85 $g\,kg^{-1}$) and NO_x (1.12–4.3 $g\,kg^{-1}$) was far less than that of CO (53–141.2 $g\,kg^{-1}$) and CO_2 (791.3–1557.9 $g\,kg^{-1}$) (Andreae and Merlet, 2001; Li et al., 2007a; Zhang et al., 2008), indicating SO_2 and NO_x were not the major gaseous pollutants emitted from biomass burning in this region. Figure 11 further compares the diurnal variations of CO and NO_x between PE3 and the normal period, respectively. It was found that there was almost no difference for diurnal variation of NO_x between the two periods, while great distinction existed for CO. During the normal period, usually two peaks would be observed at the morning (06:00–09:00 LST) and evening (17:00–20:00 LST) rush hours due to enhanced vehicular emission in big cities (Andreae et al., 2008; Tie et al., 2009). While during the biomass burning period, peaks evidently shifted to random times at around 08:00–10:00 and 14:00–16:00 LST, which could be controlled by the emission characteristics of local burning activities and transporting time from outside burning areas. The diurnal variation in this study was more or less similar as the profile based on fire observations from satellite over 15 tropical and subtropical regions (Giglio, 2007). Another distinct difference between the two periods was that the hourly CO concentrations during PE3 were all higher than the normal period, while there was negligible difference for NO_x, precluding the possible enhancement of vehicle emission to cause the increase of CO. The results above suggested that it might be possible to use the ratio of CO/NO_x to distinguish between biomass burning from the other emission sources. Figure 10 shows the calculated average CO/NO_x ratios during four periods. This ratio was close among NP, PE1, and PE2, which ranged between 9 and 10, while this ratio was

ACPD
11, 21713–21767, 2011

much higher during PE3 with average value of 14. During the non-biomass-burning period, CO and NO_x mainly derived from stationary (industry) and mobile (transportation) sources. No matter what type dominated the pollution, i.e. secondary inorganic aerosol, dust aerosol, or the normal period, the emission factors of fossil fuels wouldn't change much, thus the emission amounts of specific pollutants should almost be proportional regardless of the total emissions. That's why we could find that the CO/NO_x ratio didn't vary much among NP, PE1, and PE2. As viewed from the emission inventory, it was calculated that the CO/NO_x ratio of the TRACE-P non-biomass-burning inventory (i.e. sum of transportation, industry, domestic, large and small power plants emission inventory) (Streets et al., 2003) was 7 for the grid cell of YRD , very close to the measurement results of this study. While the CO/NO_x ratio of the biomass emission inventory was much higher of 24. By using a simple mixing model, in which the CO/NO_x ratio in non-biomass-burning and in biomass burning period was assumed to be 7 and 24, respectively, we could roughly estimate that biomass burning accounted for a significant contribution of about 41 % to the total CO emission in this study.

3.6 Formation mechanisms of different types of haze

Correlation analysis could shed some light on the mechanisms of haze formation under different conditions. Figure 12 demonstrates the linear relationship between gaseous pollutants (SO_2, NO_x and CO) and particulate matters ($PM_{2.5}$). During PE1, significant correlations were observed among all the three gaseous species and $PM_{2.5}$ with correlation coefficients (R) larger than 0.70 (Fig. 12a–c). As precursors of sulfate and nitrate, the good correlations between SO_2/NO_x and $PM_{2.5}$ were predictable, which corroborated the results that sulfate and nitrate dominated the aerosol composition during PE1. Although CO couldn't act as precursor of secondary aerosol, we still found its good correlation with $PM_{2.5}$ ($R = 0.71$). That's because CO was highly correlated with NO_x as stated above, which indirectly linked itself to $PM_{2.5}$. During PE2, there was only weak correlation between pollutant gases and aerosol (not shown in the figure), as the aerosol during this period was dominated by the minerals. Figure 12d–f show

ACPD
11, 21713–21767, 2011

the different correlation pattern for PE3 compared to PE1. As indicated by the correlation coefficients, NO_x had weak correlation with $PM_{2.5}$ ($R = 0.41$) and SO_2 even had no correlation with $PM_{2.5}$ ($R = 0.11$), suggesting secondary inorganic aerosol contributed little to aerosol formation. The significant correlation was only found between CO and $PM_{2.5}$ with high correlation coefficient of 0.80. Anyway, this correlation was different from PE1 and didn't mean vehicle or industry emission played a significant role in the aerosol formation as NO_x was weakly correlated with $PM_{2.5}$. In Sects. 3.3 and 3.5, we had demonstrated that organic aerosol accounted for a major fraction of particle mass, accompanied with high concentration of CO derived from biomass burning. Correlation between CO columns and AOD from many varied forest fire episodes overall the different time periods were found (Paton-Walsh et al., 2004). Sun et al. (2009) had ever observed that CO highly correlated with OA (organic aerosol) (R: 0.7 ~ 0.9) in several OA dominated events by using an Aerodyne High Resolution Time-of-Flight Aerosol Mass Spectrometer (HR-ToF-AMS). In this study, although there was no OC data of high time resolution available due to restrictions of instruments, we believed that CO could be regarded as proxy of organic aerosol during the biomass burning events, which indirectly linked itself to the particle formation.

4 Discussion: implication for air quality improvement in Mega-cities in China

In this study, we had identified three distinct pollution types, i.e. inorganic pollution, dust and biomass burning, during a short period of about two months, indicating the complex and miscellaneous aerosol sources in Eastern China. To identify the source types of haze pollution was the key to improve air quality and mitigate climate effects. In China, combustion of fossil fuels had always been the major causes of air pollution. Although there was a slow decrease of SO_2 emission (1994–2000) due to reduction of coal use and the switch to low-S coals (Streets et al., 2003), China's emission still dominated the totals of Asia (Streets et al., 2003; Zhang et al., 2009). While the NO_x emission increased 13.0 % due to the growth in transport which offset the decline in coal use

ACPD
11, 21713–21767, 2011

(Streets et al., 2003). As we stated above, the biggest problem for the future would be NO_x. Another key question was the important role of alkaline species on the neutralization of acids. Various studies had demonstrated that SO_4^{2-} and NO_3^- were mainly in the form of ammonium salts, i.e. $(NH_4)_2SO_4$, NH_4NO_3 and NH_4HSO_4 (Wang et al., 2005; Wang et al., 2006), indicating the important role of gaseous ammonia (NH_3) on the haze formation. However, little information on the NH_3 levels was available in China (Hu et al., 2008; Meng et al., 2010). Carmichael et al. (2003) mapped the distribution of NH_3 emission in East Asia and the high levels were mainly concentrated in southeast and northern China. There was an evident increasing trend of NH_3 emission in China since 1960s due to increases of livestock wastes, fertilizer application, and industrial emissions, of which Shanghai had the largest ammonia emission density (Sun and Wang, 1997). Model simulation showed the presence of ammonia significantly increased sulfate over polluted continental regions (Luo et al., 2007). Thus, effective controls on ammonia emission may be a good way to abate the formation of secondary inorganic components in aerosol and lower the frequency of haze occurrence.

In China, farmers usually burnt the crop residues out after the harvest season every year to fertilize soils and eliminate biofuel wastes. Biomass burning was the third largest source for BC and OC in China, only inferior to industrial and residential sources (Cao et al., 2006). As one of the world's continental scale Metro-Agro-Plexes (MAPs) (Chameides et al., 1994), the Yangtze River Delta region contributed over 20 % and 11 % of the total rice straw and wheat straw burnt in the field in China, respectively (calculated from Table 4 in Zhang et al., 2008). On a province-by-province basis, the YRD region accounted for about 10.7 % and 11.7 % of the total BC and OC emission derived from biomass burning (Cao et al., 2006). The most intense biomass burning activities usually occurred in late spring and summer seasons. HCHO maximums were observed during summer by the ACE-FTS satellite instrument in mid-to-high northern latitudes (Dufour et al., 2009) and a ten year (1996–2000) sequence of monthly mean HCHO columns over Northern and Southern China exhibited pronounced seasonal cycle with peaks from May to July (Stavrakou et al., 2009). Over the central Eastern

ACPD
11, 21713–21767, 2011

China, the open crop residue burning emission in June could account for approximately 40 % of the annual total (Yamaji et al., 2010). However, as the government's measures on prohibiting the crop residue burning in the field is not effective (Yang et al., 2008), biomass burning would be one of the important sources of haze in the YRD region in the future, especially during the harvest season.

Apart from emission sources from fossil fuel combustion and biomass burning, the impact of Asian dust on Eastern China was also non-negligible. For the dust storms that originated from the Gobi Desert in Mongolia and Inner-Mongolia, there were usually two major transport pathways. One was the eastward pathway that could influence Korea, Japan and even North America via the trans-Pacific transport. The other was the southeastward pathway that could impact large areas of Eastern China and Southern China, and even HongKong and Taiwan. The probability that dust affected northern and eastern China was estimated to be over 70 % (Zhang and Gao, 2007). Various dust events had been recorded in Eastern China, especially the YRD region. During 2002 to 2010, totally six heavily polluted days (concentration of daily average of PM_{10} higher than 420 $\mu g\,m^{-3}$, which corresponded to the China's standards of namely API higher than 300) were recorded, of which four days were affected by the transport of dust from northwestern China, which usually occurs in the spring (Fu et al., 2010). Due to the large anthropogenic emissions in Eastern China, considerable mixing of mineral dust with pollutants on the transport pathway was found. Wang et al. (2007) found that the extent of the heterogeneous reaction on dust surface increased as the distances from dust source regions increased. During an ever recorded dust event in Shanghai on 2 April 2007, an abnormal decrease of 2 pH units in dust aerosol than in non-dust aerosol was observed (Huang et al., 2010), and the similar phenomena was also observed during the 2001 TRACE-P flight observations that the pH of the dust that transported over Shanghai even reached a low value of approximate 1.00 (Meskhidze et al., 2003). On 21 March 2010, an even stronger dust event hit Shanghai and reached peak PM_{10} hourly value of 2000 $\mu g\,m^{-3}$ with the daily PM_{10} concentration of 1135 $\mu g\,m^{-3}$ (unpublished data), even worse than the ever recorded dust event in

ACPD
11, 21713–21767, 2011

2007 (Fu et al., 2010; Huang et al., 2010). This dust storm had caused the heaviest dust event in Taiwan (Taiwan EPA, http://www.epa.gov.tw/). The dust storm frequency had strong negative correlation with precipitation (Liu et al., 2004). Recent studies found that severe air pollution (including dust) could suppress precipitation (Lin et al., 2010; Min et al., 2009; Rosenfeld et al., 2007), which probably feedback higher occurrence frequency of dust storms. As dust has been the natural phenomena for thousands of years and couldn't be possibly eliminated, it will be one of the causes of haze in Eastern China in the long run, especially in spring.

5 Conclusions

An intensive aerosol and trace gases campaign was carried out over the Yangtze River Delta region in Eastern China during April to June 2009. Three pollution episodes were identified based on the atmospheric visibility, aerosol mass concentrations in different sizes, mass fraction of fine particles and modeled air trajectories. Distinct characteristics were observed among the three pollution episodes by using a synergy of ground-based measurement, satellite observation, and lidar inversion. Three typical types of air pollution for causing the haze weather in Eastern China were identified, i.e. secondary inorganic pollution, dust invasion and biomass burning.

1. During the secondary inorganic pollution episode, satellite inversion observed high AOD (>1.2) and relatively high Angstrom exponent ($0.8 \sim 1.2$) over the Eastern China region. The major components of $PM_{2.5}$ were sulfate, nitrate and ammonium. The sum of these three species reached $48.86 \pm 5.01\ \mu g\ m^{-3}$ and account for a dominant mass fraction of 77 % in $PM_{2.5}$. High concentrations of SO_2, NO_x and CO and good correlations between these trace gases and $PM_{2.5}$ indicated that anthropogenic sources (coal burning, vehicle emission etc.) were the major cause.

2. During the dust pollution episode, high AOD (>1.2) and low Angstrom exponent ($0.5 \sim 0.6$) were observed in northern and eastern China, indicating the existence

ACPD
11, 21713–21767, 2011

of considerable coarse particles. Mineral aerosol accounted for 76.8 % of the total suspended particles (TSP) and the Ca/Al elemental ratio dropped to a relatively low value of 0.75, which indicated its dust source region in Gobi Desert.

3. The biomass burning pollution episode was characteristic of high column concentrations of CO, HCHO and AOD, which were relatively consistent with regions of dense fire spots. Particulate components such as K^+, OC and EC were greatly enhanced as well as the ratio of OC/EC. The organic aerosol was estimated to account for over 50 % to PM_{10}, and the significant correlation between CO and $PM_{2.5}$ while the weak correlations between SO_2, NO_x and $PM_{2.5}$ corroborated that organic aerosol was the major species during biomass burning.

4. The enrichment factor analysis demonstrated that elements during dust pollution were least enriched while the enrichment degrees were highest during the inorganic secondary pollution. The concentration level and enrichment degree of arsenic (As) was highest during the biomass burning period. We speculated that it could be more from the biomass burning emission source other than its usual source from coal burning as the water for irrigating the crops in East Asia had been probably contaminated by arsenic pollution.

5. Lidar measurement revealed that aerosol were mainly composed of spheric particles (deplorization ratio $\delta_{532} < 5$ %) during the secondary inorganic pollution and biomass burning episodes, and vertical profile of backscattering coefficient had a sharp decrease with altitudes. While the average δ_{532} value of the boundary layer was 0.122 ± 0.023 during the dust period, indicating existence of considerable coarse particles. The dust period had a different profile from the other two periods that the dust layer contributed about 51–57 % to the total aerosol extinction at the altitude of 0.7–1.0 km, which compensated the decrease of spheric aerosol extinction.

ACPD
11, 21713–21767, 2011

Acknowledgements. Many thanks to the MODIS, OMI and AIRS data processing team members. We thank Sugimoto Nobuo and Shimizu Atsushi of National Institute for Environmental Studies, Japan for the lidar setup and data inversion. This work was supported by the great international collaboration project of MOST, China (2010DFA92230), the National Key Project of Basic Research of China (Grant Nos. 2006CB403704), and National Natural Science Foundation of China (Grant Nos. 20877020, 20977017).

References

Andreae, M. O.: Soot Carbon and Excess Fine Potassium – Long-Range Transport of Combustion-Derived Aerosols, Science, 220(4602), 1148–1151, 1983.

Andreae, M. O. and Merlet, P.: Emission of trace gases and aerosols from biomass burning, Global Biogeochem. Cy., 15(4), 955–966, 2001.

Andreae, M. O., Schmid, O., Yang, H., Chand, D., Yu, J. Z., Zeng, L. M., and Zhang, Y. H.: Optical properties and chemical composition of the atmospheric aerosol in urban Guangzhou, China, Atmos. Environ., 42(25), 6335–6350, 2008.

Arimoto, R., Duce, R. A., Savoie, D. L., Prospero, J. M., Talbot, R., Cullen, J. D., Tomza, U., Lewis, N. F., and Jay, B. J.: Relationships among aerosol constituents from Asia and the North Pacific during PEM-West A, J. Geophys. Res., 101, 2011–2023, 1996.

Boian, C. and Kirchhoff, V. W. J. H.: Measurements of CO in an aircraft experiment and their correlation with biomass burning and air mass origin in South America, Atmos. Environ., 38(37), 6337–6347, 2004.

Brammer, H. and Ravenscroft, P.: Arsenic in groundwater: A threat to sustainable agriculture in South and South-east Asia, Environ. Int., 35(3), 647–654, 2009.

Cai, H. and Xie, S. D.: Estimation of vehicular emission inventories in China from 1980 to 2005, Atmos. Environ., 41(39), 8963–8979, 2007.

Cao, G. L., Zhang, X. Y., and Zheng, F. C.: Inventory of black carbon and organic carbon emissions from China, Atmos. Environ., 40(34), 6516–6527, 2006.

Cao, T., An, L., Wang, M., Lou, Y. X., Yu, Y. H., Wu, J. M., Zhu, Z. R., Qing, Y. K., and Glime, J.: Spatial and temporal changes of heavy metal concentrations in mosses and its indication to the environments in the past 40 years in the city of Shanghai, China, Atmos. Environ., 42(21), 5390–5402, 2008.

ACPD

11, 21713–21767, 2011

Carmichael, G. R., Ferm, M., Thongboonchoo, N., Woo, J. H., Chan, L. Y., Murano, K., Viet, P. H., Mossberg, C., Bala, R., Boonjawat, J., Upatum, P., Mohan, M., Adhikary, S. P., Shrestha, A. B., Pienaar, J. J., Brunke, E. B., Chen, T., Jie, T., Guoan, D., Peng, L. C., Dhiharto, S., Harjanto, H., Jose, A. M., Kimani, W., Kirouane, A., Lacaux, J. P., Richard, S., Barturen, O., Cerda, J. C., Athayde, A., Tavares, T., Cotrina, J. S., and Bilici, E.: Measurements of sulfur dioxide, ozone and ammonia concentrations in Asia, Africa, and South America using passive samplers, Atmos. Environ., 37(9–1)0, 1293–1308, 2003.

Cass, G. R.: On the relationship between sulfate air quality and visibility with examples in los angeles, Atmos. Environ., 13(8), 1069–1084, 1979.

Chakrabarty, R. K., Moosmuller, H., Garro, M. A., Arnott, W. P., Walker, J., Susott, R. A., Babbitt, R. E., Wold, C. E., Lincoln, E. N., and Hao, W. M.: Emissions from the laboratory combustion of wildland fuels: Particle morphology and size, J. Geophys. Res., 111, D07204, doi:10.1029/2005JD006659, 2006.

Chameides, W. L., Kasibhatla, P. S., Yienger, J., and Levy, H.: Growth of Continental-Scale Metro-Agro-Plexes, Regional Ozone Pollution, and World Food-Production, Science, 264(5155), 74–77, 1994.

Chan, C. K. and Yao, X.: Air pollution in mega cities in China, Atmos. Environ., 42(1), 1–42, 2008.

Chan, Y. C., Simpson, R. W., McTainsh, G. H., Vowles, P. D., Cohen, D. D., and Bailey, G. M.: Source apportionment of visibility degradation problems in Brisbane (Australia) using the multiple linear regression techniques, Atmos. Environ., 33(19), 3237–3250, 1999.

Chang, D. and Song, Y.: Estimates of biomass burning emissions in tropical Asia based on satellite-derived data, Atmos. Chem. Phys., 10, 2335–2351, doi:10.5194/acp-10-2335-2010, 2010.

Chang, D., Song, Y., and Liu, B.: Visibility trends in six megacities in China 1973–2007, Atmos. Res., 94(2), 161–167, 2009.

Che, H. Z., Shi, G. Y., Zhang, X. Y., Arimoto, R., Zhao, J. Q., Xu, L., Wang, B., and Chen, Z. H.: Analysis of 40 years of solar radiation data from China, 1961–2000, Geophys. Res. Lett., 32, L06803, doi:10.1029/2004GL022322, 2005.

Che, H. Z., Zhang, X. Y., Li, Y., Zhou, Z. J., and Qu, J. J.: Horizontal visibility trends in China 1981–2005, Geophys. Res. Lett., 34, L24706, doi:10.1029/2007GL031450, 2007.

Chen, C. H., Wang, B. Y., Fu, Q. Y., Green, C., and Streets, D. G.: Reductions in emissions of local air pollutants and co-benefits of Chinese energy policy: a Shanghai case study, Energy

ACPD
11, 21713–21767, 2011

Policy, 34(6), 754–762, 2006.
Chen, J. M., Tan, M. G., Li, Y. L., Zhang, Y. M., Lu, W. W., Tong, Y. P., Zhang, G. L., and Li, Y.: A lead isotope record of shanghai atmospheric lead emissions in total suspended particles during the period of phasing out of leaded gasoline, Atmos. Environ., 39(7), 1245–1253, 2005.
Choi, S. D. and Chang, Y. S.: Carbon monoxide monitoring in Northeast Asia using MOPITT: Effects of biomass burning and regional pollution in April 2000, Atmos. Environ., 40(4), 686–697, 2006.
Chow, J. C. and Watson, J. G.: $PM_{2.5}$ carbonate concentrations at regionally representative Interagency Monitoring of Protected Visual Environment sites, J. Geophys. Res., 107(D21), 8344, doi:10.1029/2001JD000574, 2002.
Chu, D. A., Kaufman, Y. J., Zibordi, G., Chern, J. D., Mao, J., Li, C. C., and Holben, B. N.: Global monitoring of air pollution over land from the Earth Observing System-Terra Moderate Resolution Imaging Spectroradiometer (MODIS), J. Geophys. Res., 108(D21), 466, doi:10.1029/2002JD003179, 2003.
Crutzen, P. J. and Andreae, M. O.: Biomass Burning in the Tropics – Impact on Atmospheric Chemistry and Biogeochemical Cycles, Science, 250(4988), 1669–1678, 1990.
Deng, C., Zhuang, G., Huang, K., Li, J., Zhang, R., Wang, Q., Liu, T., Sun, Y., Guo, Z., Fu, J. S., and Wang, Z.: Chemical characterization of aerosols at the summit of Mountain Tai in Central East China, Atmos. Chem. Phys., 11, 7319–7332, doi:10.5194/acp-11-7319-2011, 2011.
Dufour, G., Szopa, S., Barkley, M. P., Boone, C. D., Perrin, A., Palmer, P. I., and Bernath, P. F.: Global upper-tropospheric formaldehyde: seasonal cycles observed by the ACE-FTS satellite instrument, Atmos. Chem. Phys., 9, 3893–3910, doi:10.5194/acp-9-3893-2009, 2009.
Fang, M., Chan, C. K., and Yao, X. H.: Managing air quality in a rapidly developing nation: China, Atmos. Environ., 43(1), 79–86, 2009.
Feng, J. L., Hu, M., Chan, C. K., Lau, P. S., Fang, M., He, L. Y., and Tang, X. Y.: A comparative study of the organic matter in $PM_{2.5}$ from three Chinese megacities in three different climatic zones, Atmos. Environ., 40(21), 3983–3994, 2006.
Feng, Y. L., Chen, Y. J., Guo, H., Zhi, G. R., Xiong, S. C., Li, J., Sheng, G. Y., and Fu, J. M.: Characteristics of organic and elemental carbon in $PM_{2.5}$ samples in Shanghai, China, Atmos. Res., 92(4), 434–442, 2009.
Fernald, F. G.: Analysis of Atmospheric Lidar Observations - Some Comments, Appl. Opt.,

ACPD
11, 21713–21767, 2011

23(5), 652–653, 1984.
Fu, Q. Y., Zhuang, G. S., Wang, J., Xu, C., Huang, K., Li, J., Hou, B., Lu, T., and Streets, D. G.: Mechanism of formation of the heaviest pollution episode ever recorded in the Yangtze River Delta, China, Atmos. Environ., 42(9), 2023–2036, 2008.
Fu, Q. Y., Zhuang, G. S., Li, J. A., Huang, K., Wang, Q. Z., Zhang, R., Fu, J., Lu, T., Chen, M., Wang, Q. A., Chen, Y., Xu, C., and Hou, B.: Source, long-range transport, and characteristics of a heavy dust pollution event in Shanghai, J. Geophys. Res., 115, D00K29, doi:10.1029/2009JD013208, 2010.
Gao, J., Wang, T., Zhou, X. H., Wu, W. S., and Wang, W. X.: Measurement of aerosol number size distributions in the Yangtze River delta in China: Formation and growth of particles under polluted conditions, Atmos. Environ., 43(4), 829–836, 2009.
Garland, R. M., Yang, H., Schmid, O., Rose, D., Nowak, A., Achtert, P., Wiedensohler, A., Takegawa, N., Kita, K., Miyazaki, Y., Kondo, Y., Hu, M., Shao, M., Zeng, L. M., Zhang, Y. H., Andreae, M. O., and Pöschl, U.: Aerosol optical properties in a rural environment near the mega-city Guangzhou, China: implications for regional air pollution, radiative forcing and remote sensing, Atmos. Chem. Phys., 8, 5161–5186, doi:10.5194/acp-8-5161-2008, 2008.
Geng, F. H., Zhang, Q., Tie, X. X., Huang, M. Y., Ma, X. C., Deng, Z. Z., Yu, Q., Quan, J. N., and Zhao, C. S.: Aircraft measurements of O-3, NO_x, CO, VOCs, and SO2 in the Yangtze River Delta region, Atmos. Environ., 43(3), 584–593, 2009.
Giglio, L.: Characterization of the tropical diurnal fire cycle using VIRS and MODIS observations, Remote Sens. Environ., 108(4), 407–421, 2007.
Groblicki, P. J., Wolff, G. T., and Countess, R. J.: Visibility-Reducing Species in the Denver Brown Cloud, 1. Relationships between Extinction and Chemical-Composition, Atmos. Environ., 15(12), 2473–2484, 1981.
Hasan, H. and Dzubay, T. G.: Apportioning Light Extinction Coefficients to Chemical-Species in Atmospheric Aerosol, Atmos. Environ., 17(8), 1573–1581, 1983.
He, Y., Uno, I., Wang, Z., Ohara, T., Sugirnoto, N., Shimizu, A., Richter, A., and Burrows, J. P.: Variations of the increasing trend of tropospheric NO_2 over central east China during the past decade, Atmos. Environ., 41(23), 4865–4876, 2007.
Hu, M., Wu, Z. J., Slanina, J., Lin, P., Liu, S., and Zeng, L. M.: Acidic gases, ammonia and water-soluble ions in $PM_{2.5}$ at a coastal site in the Pearl River Delta, China, Atmos. Environ., 42(25), 6310–6320, 2008.
Huang, K., Zhuang, G. S., Xu, C., Wang, Y., and Tang, A. H.: The chemistry of the severe acidic

ACPD
11, 21713–21767, 2011

precipitation in Shanghai, China, Atmos. Res., 89(1–2), 149–160, 2008.
Huang, K., Zhuang, G. S., Li, J. A., Wang, Q. Z., Sun, Y. L., Lin, Y. F., and Fu, J. S.: Mixing of Asian dust with pollution aerosol and the transformation of aerosol components during the dust storm over China in spring 2007, J. Geophys. Res., 115, D00K13, doi:10.1029/2009JD013145, 2010.
Kaiser, D. P. and Qian, Y.: Decreasing trends in sunshine duration over China for 1954-1998: Indication of increased haze pollution?, Geophys. Res. Lett., 29(21), 2042, doi:10.1029/2002GL016057, 2002.
Kan, H. D. and Chen, B. H.: Particulate air pollution in urban areas of Shanghai, China: health-based economic assessment, Sci. Total Environ., 322(1–3), 71–79, 2004.
Kan, H. D., London, S. J., Chen, G. H., Zhang, Y. H., Song, G. X., Zhao, N. Q., Jiang, L. L., and Chen, B. H.: Differentiating the effects of fine and coarse particles on daily mortality in Shanghai, China, Environ. Int., 33(3), 376–384, 2007.
Kato, S., Akimoto, H., Rockmann, T., Braunlich, M., and Brenninkmeijer, C. A. M.: Stable isotopic compositions of carbon monoxide from biomass burning experiments, Atmos. Environ., 33(27), 4357–4362, 1999.
Kato, S., Pochanart, P., Hlrokawa, J., Kajii, Y., Akimoto, H., Ozaki, Y., Obi, K., Katsuno, T., Streets, D. G., and Minko, N. P.: The influence of Siberian forest fires on carbon monoxide concentrations at Happo, Japan, Atmos. Environ., 36(2), 385–390, 2002.
Kaufman, Y. J., Wald, A. E., Remer, L. A., Gao, B. C., Li, R. R., and Flynn, L.: The MODIS 2.1-mu m channel – Correlation with visible reflectance for use in remote sensing of aerosol, Ieee T. Geosci. Remote Sens., 35(5), 1286–1298, 1997.
Kim, S. W., Yoon, S. C., Kim, J., Kang, J. Y., and Sugimoto, N.: Asian dust event observed in Seoul, Korea, during 29–31 May 2008: Analysis of transport and vertical distribution of dust particles from lidar and surface measurements, Sci. Total Environ., 408(7), 1707–1718, 2010.
Kurosu, T. P., Chance, K., and Sioris, C. E.: Preliminary Results for HCHO and BrO from the EOS-Aura Ozone Monitoring Instrument, Passive Optical Remote Sensing of the Atmosphere and Clouds IV, edited by: Tsay, S. C., Yokota, T., and Ahn, M.-H., Proc. of SPIE, Vol. 5652, 2004.
Lee, S., Ghim, Y. S., Kim, S. W., and Yoon, S. C.: Seasonal characteristics of chemically apportioned aerosol optical properties at Seoul and Gosan, Korea, Atmos. Environ., 43(6), 1320–1328, 2009.

ACPD
11, 21713–21767, 2011

Levelt, P. F., Van den Oord, G. H. J., Dobber, M. R., Malkki, A., Visser, H., de Vries, J., Stammes, P., Lundell, J. O. V., and Saari, H.: The Ozone Monitoring Instrument, Ieee T. Geosci. Remote Sens., 44(5), 1093–1101, 2006.

Li, J., Posfai, M., Hobbs, P. V., and Buseck, P. R.: Individual aerosol particles from biomass burning in southern Africa: 2, Compositions and aging of inorganic particles, J. Geophys. Res., 108(D13), 8484, doi:10.1029/2002JD002310, 2003.

Li, X. G., Wang, S. X., Duan, L., Hao, J., Li, C., Chen, Y. S., and Yang, L.: Particulate and trace gas emissions from open burning of wheat straw and corn stover in China, Environ. Sci. Technol., 41(17), 6052–6058, 2007.

Li, Z. Q., Chen, H., Cribb, M., Dickerson, R., Holben, B., Li, C., Lu, D., Luo, Y., Maring, H., Shi, G., Tsay, S. C., Wang, P., Wang, Y., Xia, X., Zheng, Y., Yuan, T., and Zhao, F.: Preface to special section on east Asian studies of tropospheric aerosols: An international regional experiment (EAST-AIRE), J. Geophys. Res., 112, D22S00, doi:10.1029/2007JD008853, 2007.

Lin, Y. F., Min, Q. L., Zhuang, G. S., Wang, Z. W., Gong, W., and Li, R.: Spatial features of rain frequency change induced by pollution and associated aerosols, Atmos. Chem. Phys. Discuss., 10, 14495–14511, doi:10.5194/acpd-5110-14495-12010, 2010.

Liu, F., Wang, X. K., and Zhu, Y. G.: Assessing current and future ozone-induced yield reductions for rice and winter wheat in Chongqing and the Yangtze River Delta of China, Environ. Pollut., 157(2), 707–709, 2009.

Liu, X. D., Yin, Z. Y., Zhang, X. Y., and Yang, X. C.: Analyses of the spring dust storm frequency of northern China in relation to antecedent and concurrent wind, precipitation, vegetation, and soil moisture conditions, J. Geophys. Res., 109, D16210, doi:10.1029/2004JD004615, 2004.

Liu, Z., Liu, D., Huang, J., Vaughan, M., Uno, I., Sugimoto, N., Kittaka, C., Trepte, C., Wang, Z., Hostetler, C., and Winker, D.: Airborne dust distributions over the Tibetan Plateau and surrounding areas derived from the first year of CALIPSO lidar observations, Atmos. Chem. Phys., 8, 5045–5060, doi:10.5194/acp-8-5045-2008, 2008.

Liu, Z. Y., Sugimoto, N., and Murayama, T.: Extinction-to-backscatter ratio of Asian dust observed with high-spectral-resolution lidar and Raman lidar, Appl. Opt., 41(15), 2760–2767, 2002.

Luo, C., Zender, C. S., Bian, H. S., and Metzger, S.: Role of ammonia chemistry and coarse mode aerosols in global climatological inorganic aerosol distributions, Atmos. Environ., 41(12), 2510–2533, 2007.

ACPD
11, 21713–21767, 2011

Malm, W. C., Sisler, J. F., Huffman, D., Eldred, R. A., and Cahill, T. A.: Spatial and Seasonal Trends in Particle Concentration and Optical Extinction in the United-States, J. Geophys. Res.-Atmos., 99, 1347–1370, 1994.

Mandal, B. K. and Suzuki, K. T.: Arsenic round the world: a review, Talanta, 58(1), 201–235, 2002.

Marbach, T., Beirle, S., Liu, C., Platt, U., and Wagner, T.: Biomass burning emissions from satellite observations synergistic use of formaldehyde (HCHO), fire counts and surface temperature, Remote Sensing of Fire: Science and Application, edited by: Hao, W. M., Proc. of SPIE, Vol. 7089, 2008.

Mari, C. H., Cailley, G., Corre, L., Saunois, M., Attié, J. L., Thouret, V., and Stohl, A.: Tracing biomass burning plumes from the Southern Hemisphere during the AMMA 2006 wet season experiment, Atmos. Chem. Phys., 8, 3951–3961, doi:10.5194/acp-8-3951-2008, 2008.

McMillan, W. W., Barnet, C., Strow, L., Chahine, M. T., McCourt, M. L., Warner, J. X., Novelli, P. C., Korontzi, S., Maddy, E. S., and Datta, S.: Daily global maps of carbon monoxide from NASA's Atmospheric Infrared Sounder, Geophys. Res. Lett., 32, L11801, doi:10.1029/2004GL021821, 2005.

Mcneil, W. R., and Carswell, A. I.: Lidar Polarization Studies of Troposphere, Appl. Opt., 14(9), 2158–2168, 1975.

Meng, Z. Y., Xu, X. B., Wang, T., Zhang, X. Y., Yu, X. L., Wang, S. F., Lin, W. L., Chen, Y. Z., Jiang, Y. A., and An, X. Q.: Ambient sulfur dioxide, nitrogen dioxide, and ammonia at ten background and rural sites in China during 2007–2008, Atmos. Environ., 44(21–22), 2625–2631, 2010.

Meskhidze, N., Chameides, W. L., Nenes, A., and Chen, G.: Iron mobilization in mineral dust: Can anthropogenic SO_2 emissions affect ocean productivity?, Geophys. Res. Lett., 30(21), 2085, doi:2010.1029/2003GL018035, 2003.

Min, Q.-L., Li, R., Lin, B., Joseph, E., Wang, S., Hu, Y., Morris, V., and Chang, F.: Evidence of mineral dust altering cloud microphysics and precipitation, Atmos. Chem. Phys., 9, 3223–3231, doi:10.5194/acp-9-3223-2009, 2009.

Noh, Y. M., Kim, Y. J., Choi, B. C., and Murayama, T.: Aerosol lidar ratio characteristics measured by a multi-wavelength Raman lidar system at Anmyeon Island, Korea, Atmos. Res., 86(1), 76–87, 2007.

Nriagu, J. O.: A Global Assessment of Natural Sources of Atmospheric Trace-Metals, Nature, 338(6210), 47–49, 1989.

ACPD
11, 21713–21767, 2011

Ouimette, J. R. and Flagan, R. C.: The Extinction Coefficient of Multicomponent Aerosols, Atmos. Environ., 16(10), 2405–2419, 1982.
Palmer, P. I., Barkley, M. P., Kurosu, T. P., Lewis, A. C., Saxton, J. E., Chance, K., and Gatti, L. V.: Interpreting satellite column observations of formaldehyde over tropical South America, Philos. T. Roy. Soc. A-Math, 365(1856), 1741–1751, 2007.
Pan, L. A., Che, H. Z., Geng, F. H., Xia, X. G., Wang, Y. Q., Zhu, C. Z., Chen, M., Gao, W., and Guo, J. P.: Aerosol optical properties based on ground measurements over the Chinese Yangtze Delta Region, Atmos. Environ., 44(21–22), 2587–2596, 2010.
Parrish, D. D. and Zhu, T.: Clean Air for Megacities, Science, 326(5953), 674–675, 2009.
Pathak, R. K., Wu, W. S., and Wang, T.: Summertime $PM_{2.5}$ ionic species in four major cities of China: nitrate formation in an ammonia-deficient atmosphere, Atmos. Chem. Phys., 9, 1711–1722, doi:10.5194/acp-9-1711-2009, 2009.
Paton-Walsh, C., Jones, N., Wilson, S., Meier, A., Deutscher, N., Griffith, D., Mitchell, R., and Campbell, S.: Trace gas emissions from biomass burning inferred from aerosol optical depth, Geophys. Res. Lett., 31, L05116, doi:10.1029/2003GL018973, 2004.
Peundorf, R.: Tables of the refractive index for standard and the Rayleigh scattering coefficient for the spectral region between 0.2 and 20.0 microns and their application to atmospheric optics, J. Opt. Soc. Am., 47, 176–182, 1957.
Rosenfeld, D., Dai, J., Yu, X., Yao, Z. Y., Xu, X. H., Yang, X., and Du, C. L.: Inverse relations between amounts of air pollution and orographic precipitation, Science, 315(5817), 1396–1398, 2007.
Shi, G. T., Chen, Z. L., Xu, S. Y., Zhang, J., Wang, L., Bi, C. J., and Teng, J. Y.: Potentially toxic metal contamination of urban soils and roadside dust in Shanghai, China, Environ. Pollut., 156(2), 251–260, 2008.
Shimizu, A., Sugimoto, N., Matsui, I., Arao, K., Uno, I., Murayama, T., Kagawa, N., Aoki, K., Uchiyama, A., and Yamazaki, A.: Continuous observations of Asian dust and other aerosols by polarization lidars in China and Japan during ACE-Asia, J. Geophys. Res., 109, D19S17, doi:10.1029/2002JD003253, 2004.
Stavrakou, T., Müller, J.-F., De Smedt, I., Van Roozendael, M., van der Werf, G. R., Giglio, L., and Guenther, A.: Evaluating the performance of pyrogenic and biogenic emission inventories against one decade of space-based formaldehyde columns, Atmos. Chem. Phys., 9, 1037–1060, doi:10.5194/acp-9-1037-2009, 2009.
Streets, D. G., Bond, T. C., Carmichael, G. R., Fernandes, S. D., Fu, Q., He, D., Klimont, Z.,

ACPD
11, 21713–21767, 2011

Nelson, S. M., Tsai, N. Y., Wang, M. Q., Woo, J. H., and Yarber, K. F.: An inventory of gaseous and primary aerosol emissions in Asia in the year 2000, J. Geophys. Res., 108(D21), 8809, doi:10.1029/2002JD003093, 2003.

Sugimoto, N., Matsui, I., Shimizu, A., Uno, I., Asai, K., Endoh, T., and Nakajima, T.: Observation of dust and anthropogenic aerosol plumes in the Northwest Pacific with a two-wavelength polarization lidar on board the research vessel Mirai, Geophys. Res. Lett., 29(19), 1901, doi:10.1029/2002GL015112, 2002.

Sun, Q. R. and Wang, M. R.: Ammonia Emission and Concentration in the Atmosphere over China, Scientia Atmospherica Sinica, 21(5), 590–598, 1997 (in Chinese).

Sun, Y., Zhang, Q., Macdonald, A. M., Hayden, K., Li, S. M., Liggio, J., Liu, P. S. K., Anlauf, K. G., Leaitch, W. R., Steffen, A., Cubison, M., Worsnop, D. R., van Donkelaar, A., and Martin, R. V.: Size-resolved aerosol chemistry on Whistler Mountain, Canada with a high-resolution aerosol mass spectrometer during INTEX-B, Atmos. Chem. Phys., 9, 3095–3111, doi:10.5194/acp-9-3095-2009, 2009.

Sun, Y., Zhuang, G., Wang Y., Han, L., Guo, J., Mo, D., Zhang, W., Wang, Z., and Hao, Z.: The air-borne particulate pollution in Beijing – concentration, composition, distribution and sources, Atmos. Environ., 38(35), 5991–6004, 2004.

Tan, M. G., Zhang, G. L., Li, X. L., Zhang, Y. X., Yue, W. S., Chen, J. M., Wang, Y. S., Li, A. G., Li, Y., Zhang, Y. M., and Shan, Z. C.: Comprehensive study of lead pollution in Shanghai by multiple techniques, Anal. Chem., 78(23), 8044–8050, 2006.

Tie, X. X., Geng, F. H., Peng, L., Gao, W., and Zhao, C. S.: Measurement and modeling of O-3 variability in Shanghai, China: Application of the WRF-Chem model, Atmos. Environ., 43(28), 4289–4302, 2009.

Turpin, B. J. and Lim, H. J.: Species contributions to $PM_{2.5}$ mass concentrations: Revisiting common assumptions for estimating organic mass, Aerosol Sci. Technol., 35(1), 602–610, 2001.

van der A, R. J., Peters, D. H. M. U., Eskes, H., Boersma, K. F., Van Roozendael, M., De Smedt, I., and Kelder, H. M.: Detection of the trend and seasonal variation in tropospheric NO_2 over China, J. Geophys. Res., 111, D12317, doi:10.1029/2005JD006594, 2006.

Wang, H. X., Tang, X. Y., Wang, M. L., Yan, P., Wang, T., Shao, K. S., Zeng, L. M., Du, H. F., and Chen, L. M.: Characteristics of observed trace gaseous pollutants in the Yangtze Delta, Sci. China. Ser. D, 46(4), 397–404, 2003.

Wang, K. C., Dickinson, R. E., and Liang, S. L.: Clear Sky Visibility Has Decreased over Land

ACPD
11, 21713–21767, 2011

Globally from 1973 to 2007, Science, 323(5920), 1468–1470, 2009.
Wang, T., Cheung, T. F., Li, Y. S., Yu, X. M., and Blake, D. R.: Emission characteristics of CO, NO_x, SO2 and indications of biomass burning observed at a rural site in eastern China, J. Geophys. Res., 107(D12), 4157, 10.1029/2001JD000724, 2002.
Wang, T., Nie, W., Gao, J., Xue, L. K., Gao, X. M., Wang, X. F., Qiu, J., Poon, C. N., Meinardi, S., Blake, D., Wang, S. L., Ding, A. J., Chai, F. H., Zhang, Q. Z., and Wang, W. X.: Air quality during the 2008 Beijing Olympics: secondary pollutants and regional impact, Atmos. Chem. Phys., 10, 7603–7615, doi:10.5194/acp-10-7603-2010, 2010.
Wang, Y., Zhuang, G., Tang, A., Yuan, H., Sun, Y., Chen, S., and Zheng, A.: The ion chemistry and the source of $PM_{2.5}$ aerosol in Beijing, Atmos. Environ., 39(21), 3771–3784, 2005.
Wang, Y., Zhuang, G., Zhang, X. Huang, K., Xu, C., Tang, A., Chen, J., and An, Z.: The ion chemistry, seasonal cycle, and sources of $PM_{2.5}$ and TSP aerosol in Shanghai, Atmos. Environ., 40(16), 2935–2952, 2006.
Wang, Y., Zhuang, G., Tang, A., Zhang, W., Sun, Y., Wang, Z., and An, Z.: The evolution of chemical components of aerosols at five monitoring sites of China during dust storms, Atmos. Environ., 41(5), 1091–1106, 2007.
Xia, X. G., Li, Z. Q., Holben, B., Wang, P., Eck, T., Chen, H. B., Cribb, M., and Zhao, Y. X.: Aerosol optical properties and radiative effects in the Yangtze Delta region of China, J. Geophys. Res., 112, D22S12, doi:10.1029/2007JD008859 2007.
Xu, J., Bergin, M. H., Yu, X., Liu, G., Zhao, J., Carrico, C. M., and Baumann, K.: Measurement of aerosol chemical, physical and radiative properties in the Yangtze delta region of China, Atmos. Environ., 36(2), 161–173, 2002.
Yamaji, K., Li, J., Uno, I., Kanaya, Y., Irie, H., Takigawa, M., Komazaki, Y., Pochanart, P., Liu, Y., Tanimoto, H., Ohara, T., Yan, X., Wang, Z., and Akimoto, H.: Impact of open crop residual burning on air quality over Central Eastern China during the Mount Tai Experiment 2006 (MTX2006), Atmos. Chem. Phys., 10, 7353–7368, doi:10.5194/acp-10-7353-2010, 2010.
Yan, X. Y., Ohara, T., and Akimoto, H.: Bottom-up estimate of biomass burning in mainland China, Atmos. Environ., 40(27), 5262–5273, 2006.
Yang, F. M., He, K., Ye, B., Chen, X., Cha, L., Cadle, S. H., Chan, T., and Mulawa, P. A.: One-year record of organic and elemental carbon in fine particles in downtown Beijing and Shanghai, Atmos. Chem. Phys., 5, 1449–1457, doi:10.5194/acp-5-1449-2005, 2005a.
Yang, F. M., Ye, B. M., He, K. B., Ma, Y. L., Cadle, S. H., Chan, T., and Mulawa, P. A.: Characterization of atmospheric mineral components of $PM_{2.5}$ in Beijing and Shanghai, China, Sci.

ACPD
11, 21713–21767, 2011

Total Environ., 343(1–3), 221–230, 2005b.
Yang, S. J., He, H. P., Lu, S. L., Chen, D., and Zhu, J. X.: Quantification of crop residue burning in the field and its influence on ambient air quality in Suqian, China, Atmos. Environ., 42(9), 1961–1969, 2008.
Yao, X. H., Chan, C. K., Fang, M., Cadle, S., Chan, T., Mulawa, P., He, K. B., and Ye, B. M.: The water-soluble ionic composition of $PM_{2.5}$ in Shanghai and Beijing, China, Atmos. Environ., 36(26), 4223–4234, 2002.
Ye, B. M., Ji, X. L., Yang, H. Z., Yao, X. H., Chan, C. K., Cadle, S. H., Chan, T., and Mulawa, P. A.: Concentration and chemical composition of $PM_{2.5}$ in Shanghai for a 1-year period, Atmos. Environ., 37(4), 499–510, 2003.
Ye, S. H., Zhou, W., Song, J., Peng, B. C., Yuan, D., Lu, Y. M., and Qi, P. P.: Toxicity and health effects of vehicle emissions in Shanghai, Atmos. Environ., 34(3), 419–429, 2000.
Yuan, H., Wang, Y., and Zhuang, G.: Simultaneous determination of organic acids, methanesulfonic acid and inorganic anions in aerosol and precipitation samples by ion chromatography, J. Inst. Analysis, 22, 11–44, 2003(in Chinese).
Zhang, H. F., Ye, X. N., Cheng, T. T., Chen, J. M., Yang, X., Wang, L., and Zhang, R. Y.: A laboratory study of agricultural crop residue combustion in China: Emission factors and emission inventory, Atmos. Environ., 42(36), 8432–8441, 2008.
Zhang, K. and Gao, H. W.: The characteristics of Asian-dust storms during 2000–2002: From the source to the sea, Atmos. Environ., 41(39), 9136–9145, 2007.
Zhang, Q., Streets, D. G., Carmichael, G. R., He, K. B., Huo, H., Kannari, A., Klimont, Z., Park, I. S., Reddy, S., Fu, J. S., Chen, D., Duan, L., Lei, Y., Wang, L. T., and Yao, Z. L.: Asian emissions in 2006 for the NASA INTEX-B mission, Atmos. Chem. Phys., 9, 5131–5153, doi:10.5194/acp-9-5131-2009, 2009.
Zhang, W. J., Zhuang, G. S., Huang, K., Li, J. A., Zhang, R., Wang, Q. Z., Sun, Y. L., Fu, J. S., Chen, Y., Xu, D. Q., and Wang, W.: Mixing and transformation of Asian dust with pollution in the two dust storms over the northern China in 2006, Atmos. Environ., 44(28), 3394–3403, 2010.
Zhang, X. Y., Gong, S. L., Shen, Z. X., Mei, F. M., Xi, X. X., Liu, L. C., Zhou, Z. J., Wang, D., Wang, Y. Q., and Cheng, Y.: Characterization of soil dust aerosol in China and its transport and distribution during 2001 ACE-Asia: 1. Network observations, J. Geophys. Res.-Atmos., 108(D9), 4261, doi:10.1029/2002JD002632, 2003.
Zhang, X. Y., Wang, Y. Q., Zhang, X. C., Guo, W., and Gong, S. L.: Carbonaceous aerosol

ACPD
11, 21713–21767, 2011

composition over various regions of China during 2006, J. Geophys. Res., 113, D14111, doi:10.1029/2007JD009525, 2008.
Zhang, X. Y., Zhang, P., Zhang, Y., Li, X. J., and Qiu, H.: The trend, seasonal cycle, and sources of tropospheric NO_2 over China during 1997–2006 based on satellite measurement, Sci. China. Ser. D, 50(12), 1877–1884, 2007.
Zhang, X. Y., Zhuang, G. Y., Zhu, G. H., Zhang, D., An, Z. S., Chen, T., and Huang, X. P.: Element tracers for Chinese source dust, Science in China (Series D), 39(5), 512–521, 1996.
Zhang, Y. H., Hu, M., Zhong, L. J., Wiedensohler, A., Liu, S. C., Andreae, M. O., Wang, W., and Fan, S. J.: Regional Integrated Experiments on Air Quality over Pearl River Delta 2004 (PRIDE-PRD2004): Overview, Atmos. Environ., 42(25), 6157–6173, 2008.
Zhang, Y. P., Wang, X. F., Chen, H., Yang, X., Chen, J. M., and Allen, J. O.: Source apportionment of lead-containing aerosol particles in Shanghai using single particle mass spectrometry, Chemosphere, 74(4), 501–507, 2009.
Zhao, X. S., Wan, Z., Zhu, H. G., and Chen, R. P.: The carcinogenic potential of extractable organic matter from urban airborne particles in Shanghai, China, Mutat. Res.-Gen. Tox. En., 540(1), 107–117, 2003.
Zhou, X. H., Cao, J., Wang, T., Wu, W. S., and Wang, W. X.: Measurement of black carbon aerosols near two Chinese megacities and the implications for improving emission inventories, Atmos. Environ., 43(25), 3918–3924, 2009.
Zhou, Y., Fu, J. S., Zhuang, G. S., and Levy, J. I.: Risk-Based Prioritization among Air Pollution Control Strategies in the Yangtze River Delta, China, Environ. Health Perspect., 118(9), 1204–1210, 2010.
Zhuang, G. S., Guo, J. H., Yuan, H., and Zhao, C. Y.: The compositions, sources, and size distribution of the dust storm from China in spring of 2000 and its impact on the global environment, Chinese Science Bulletin, 46(11), 895–901, 2001.

ACPD
11, 21713–21767, 2011

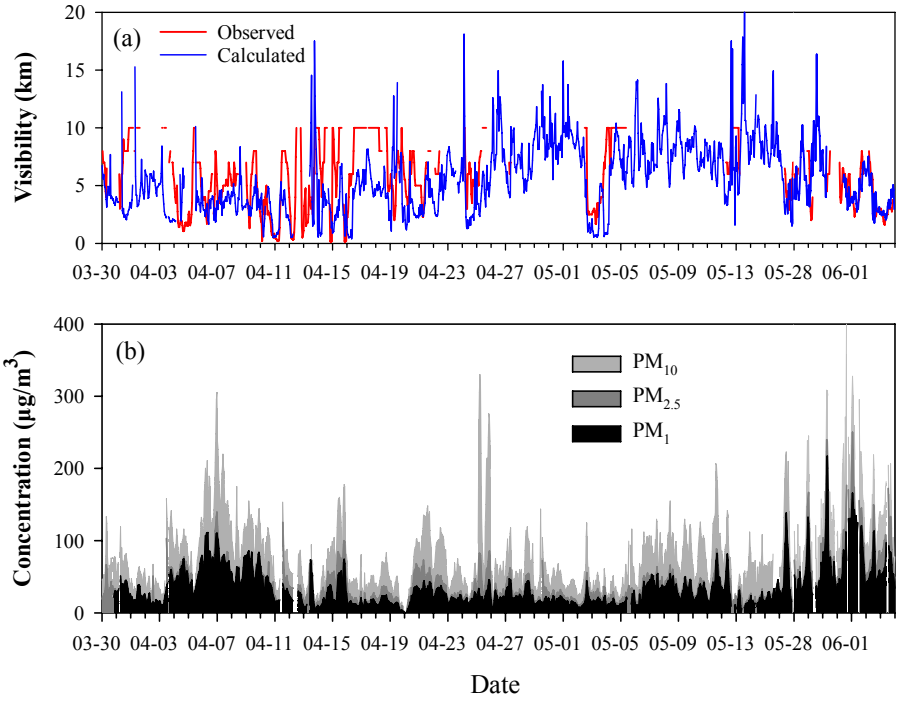

Fig. 1. (a) Time-series of the calculated and observed hourly visibility (km) during the study period (30 March ~ 16 May and 28 May ~ 3 June) in 2009 over Shanghai. The observed visibility recorded at Pudong had an upper limit of 10 km (Data source: http://www.wunderground.com). The method of calculating the visibility was described in the text. **(b)** Time-series of the hourly particulate concentrations of PM_1, $PM_{2.5}$ and PM_{10} ($\mu g\,m^{-3}$) during the same study period as above.

ACPD
11, 21713–21767, 2011

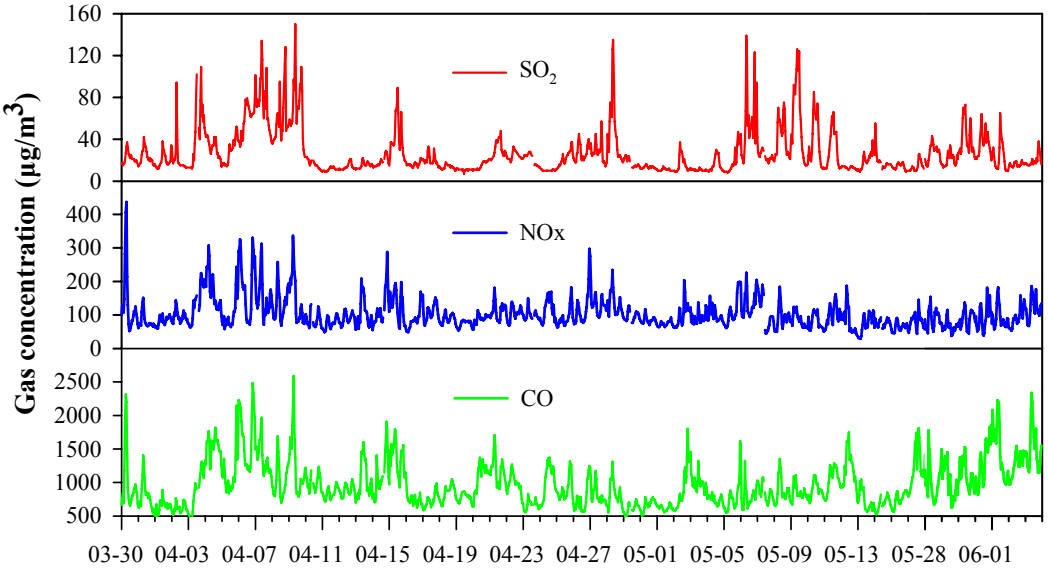

Fig. 2. Time-series of the hourly gaseous concentrations of SO_2, NOx and CO, all units are in $\mu g\,m^{-3}$.

ACPD
11, 21713–21767, 2011

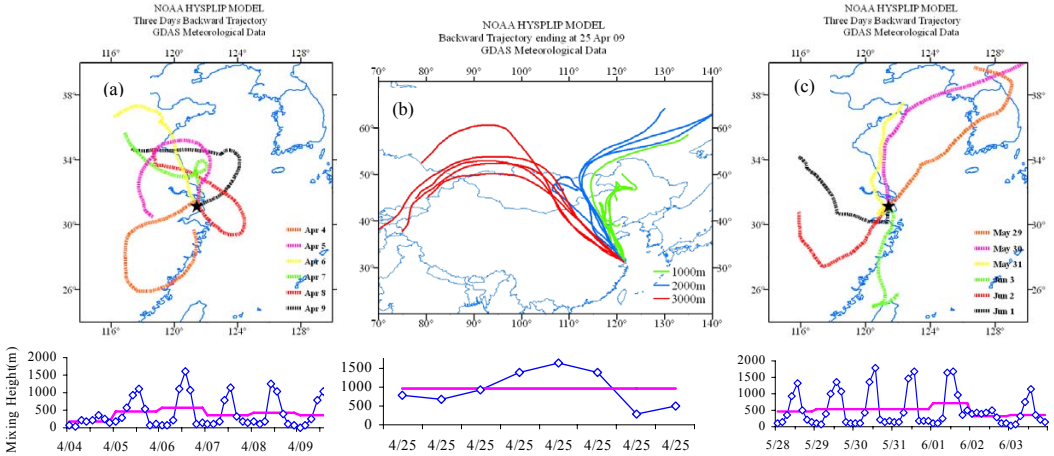

Fig. 3. Three days air mass backward trajectory at Shanghai computed by the NOAA Hybrid Single-Particle Lagrangian Trajectory (HYSPLIT) model during **(a)** PE1, **(b)** PE2, and **(c)** PE3, respectively. The starting altitude during PE1 and PE3 was 500 m and three altitudes of 500, 1000 and 1500 m were computed during PE2. The mixing heights during three episodes were shown below the trajectory panel (blue dots denoted the 3-h average mixing height and the pink horizontal step lines denoted the daily average mixing height).

ACPD
11, 21713–21767, 2011

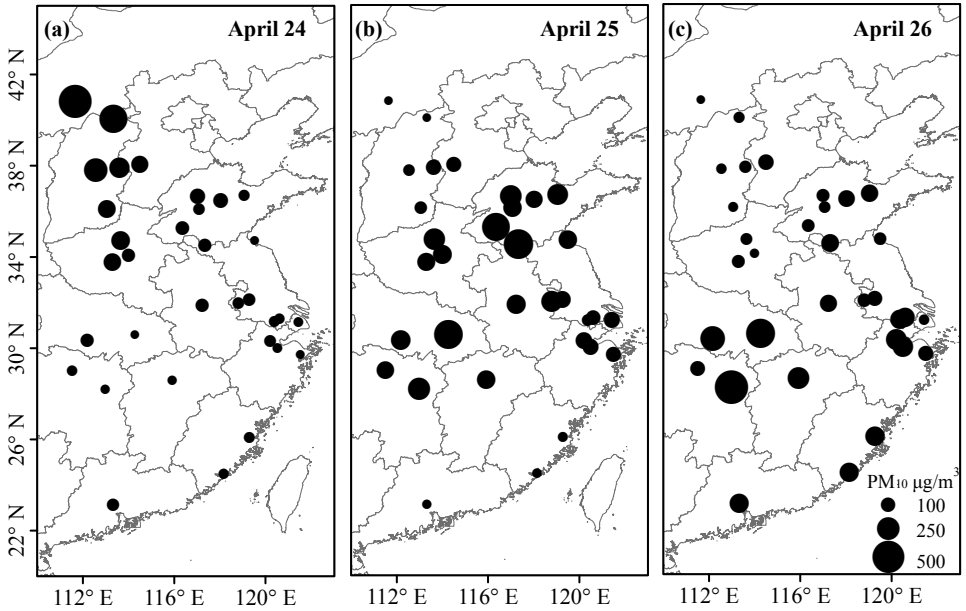

Fig. 4. Regional distribution of PM_{10} concentration ($\mu g\,m^{-3}$) during 24–26 April (Data source: Ministry of Environment Protection of the PRC, http://www.zhb.gov.cn/).

ACPD
11, 21713–21767, 2011

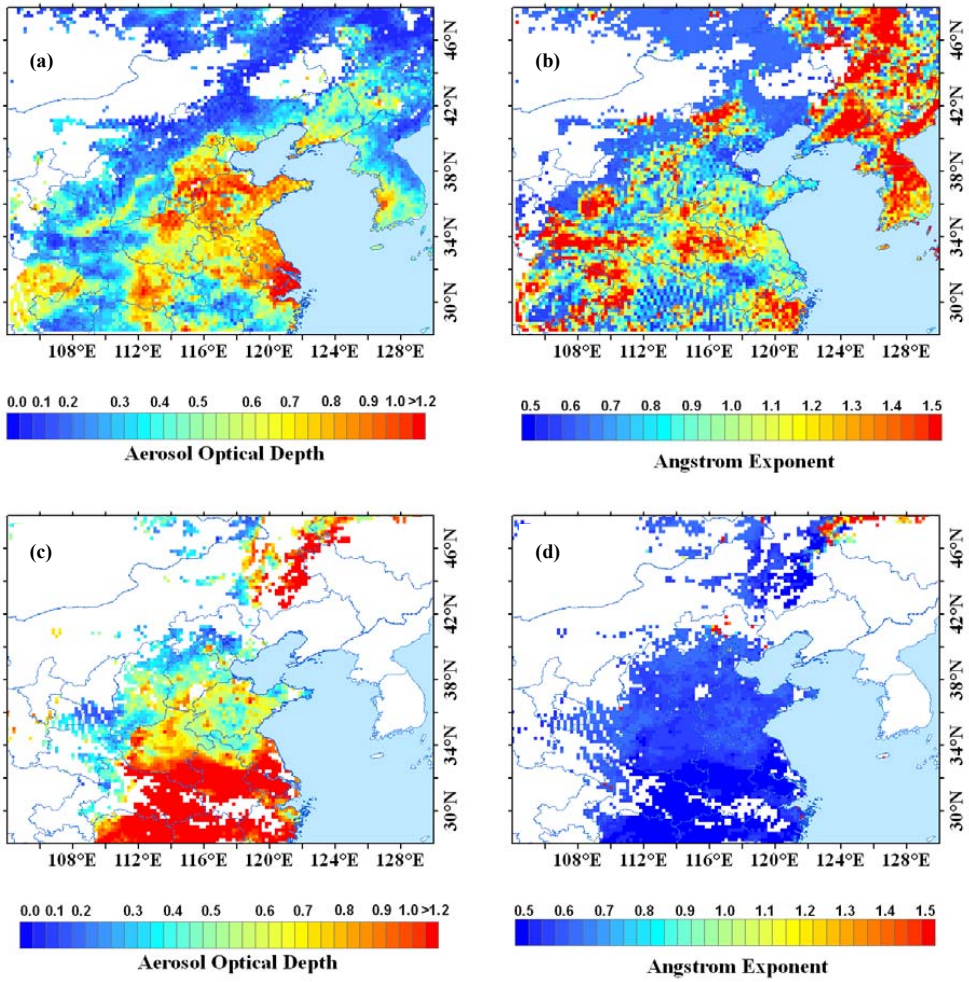

Fig. 5. Caption on next page.

ACPD
11, 21713–21767, 2011

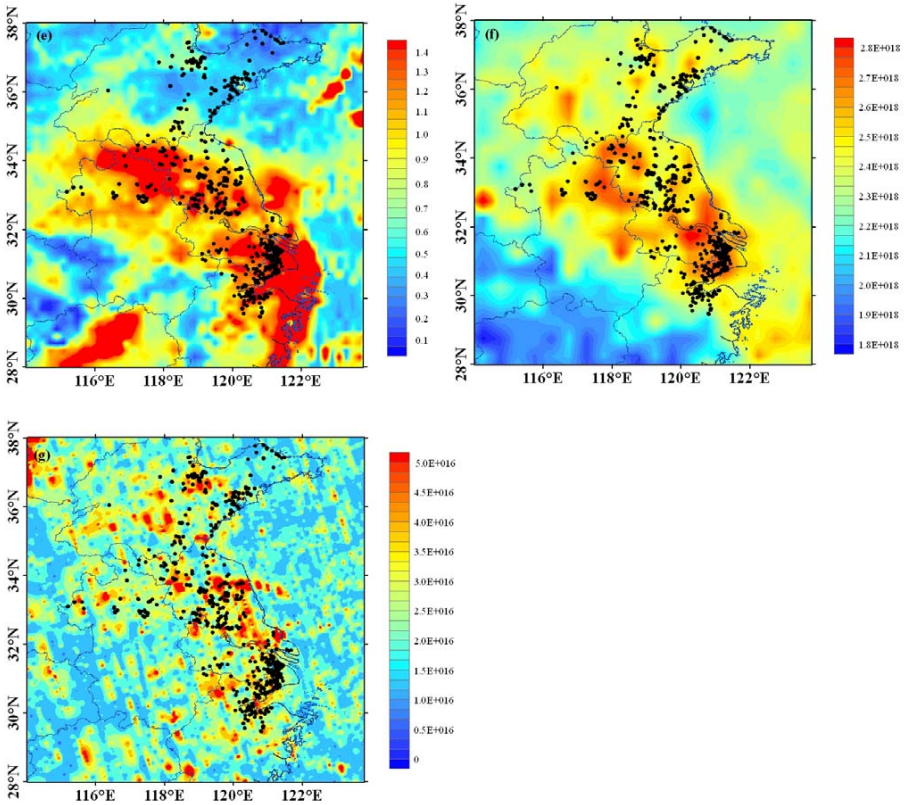

Fig. 5. The regional distribution of **(a)** aerosol optical depth (550 nm), and **(b)** Ångström exponent (470–670 nm) retrieved from MODIS during PE1; **(c)** aerosol optical depth, and **(d)** Ångström exponent during PE2; **(e)** aerosol optical depth, **(f)** total CO column concentration (molecules cm^{-2}) retrieved from AIRS, and **(g)** total formaldehyde column concentration (molecules cm^{-2}) retrieved from OMI during PE3, respectively. Total fire spots (black dots in the figure) retrieved from MODIS were plotted during PE3.

ACPD
11, 21713–21767, 2011

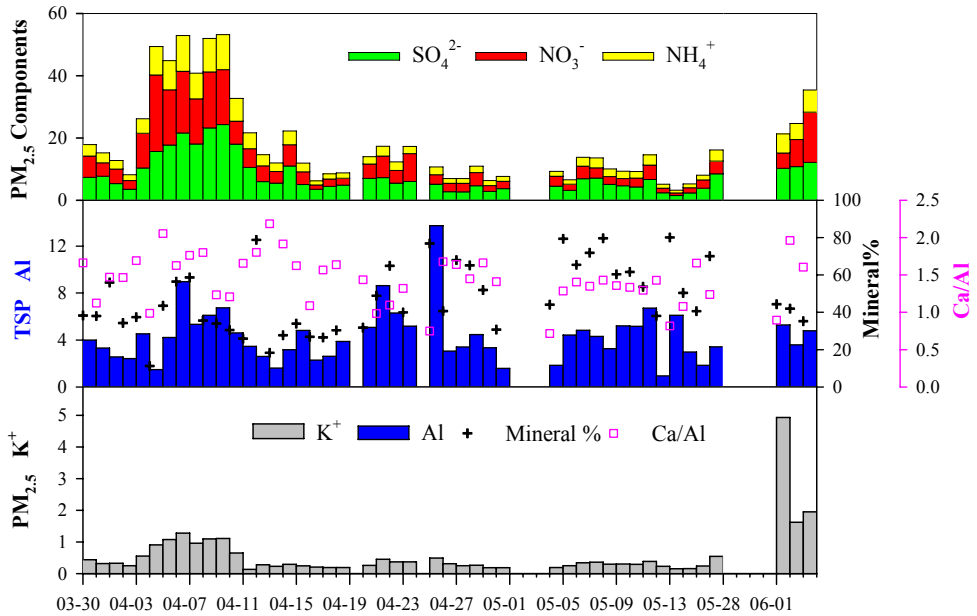

Fig. 6. Time series of **(a)** SO_4^{2-}, NO_3^-, and NH_4^+ concentration ($\mu g\,m^{-3}$) in $PM_{2.5}$ **(b)** Al concentration ($\mu g\,m^{-3}$), the fraction of mineral aerosol, and the elemental ratio of Ca/Al in the total suspended particles (TSP) **(c)** K^+ in $PM_{2.5}$, during the whole study period (Missing data were due to rainfall or malfunction of instruments).

ACPD
11, 21713–21767, 2011

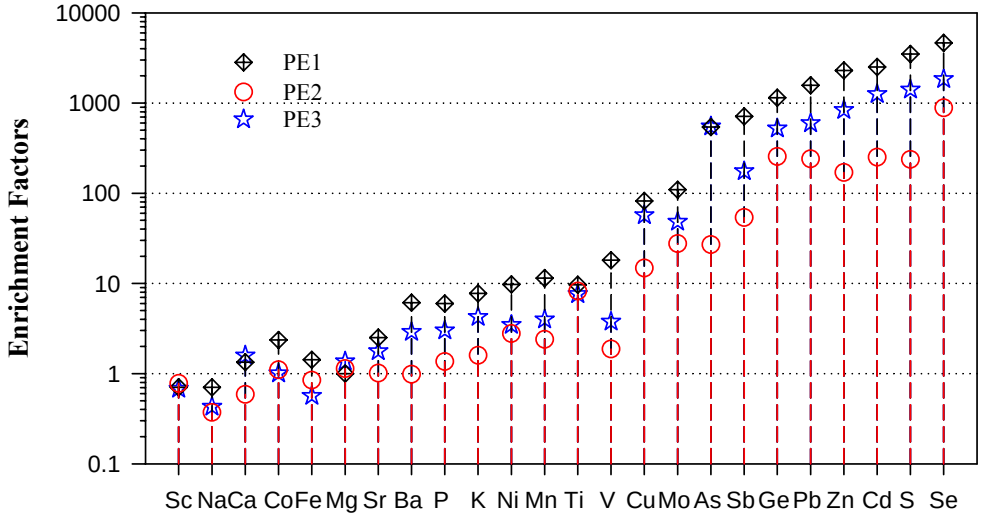

Fig. 7. The average enrichment factors (EF) of various elements during PE1, PE2, and PE3, respectively.

ACPD
11, 21713–21767, 2011

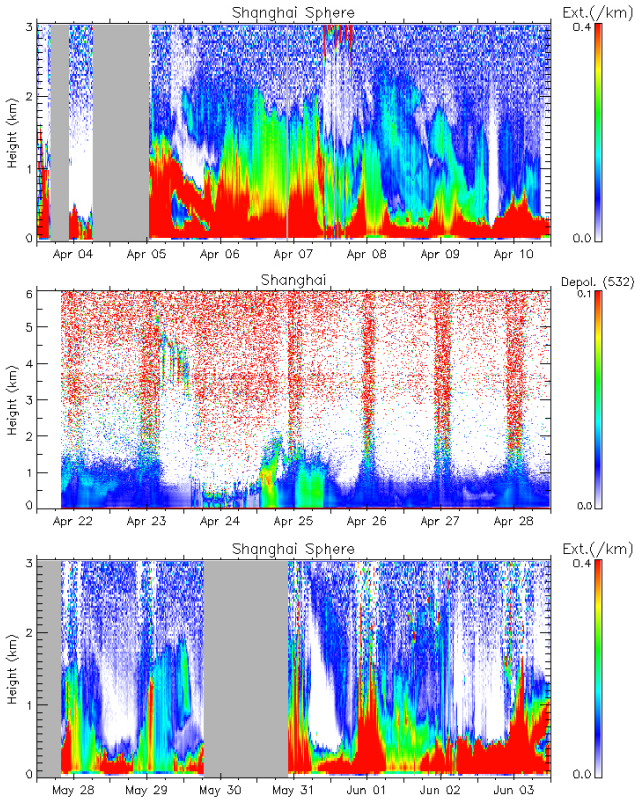

Fig. 8. Top panel: the time-height cross section of spheric aerosol extinction coefficient (km^{-1}) during PE1. Middle panel: the time-height cross section of depolarization ratio from 22–28 April, including PE2 (25 April). Bottom panel: the time-height cross section of spheric aerosol extinction coefficient (km^{-1}) during PE3. The gray columns represented the missing data which were due to the malfunction of the lidar instrument.

ACPD
11, 21713–21767, 2011

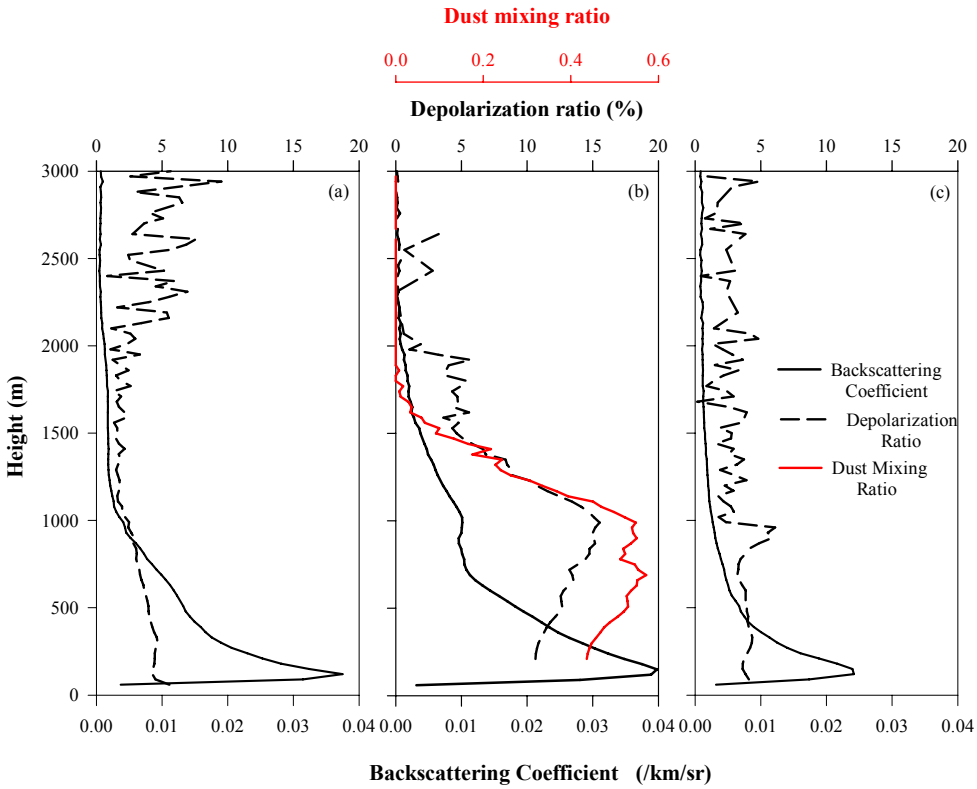

Fig. 9. Vertical profile of backscattering coefficient ($km^{-1}\,sr^{-1}$) and depolarization ratio (%) during **(a)** PE1 (6 April), **(b)** PE2 (01:30–08:00 LST, 25 April), and **(c)** PE3 (1 June). The profile of the fraction of dust aerosol extinction to the total aerosol extinction (dust mixing ratio) was calculated and presented during PE2 (Fig. 9b).

ACPD
11, 21713–21767, 2011

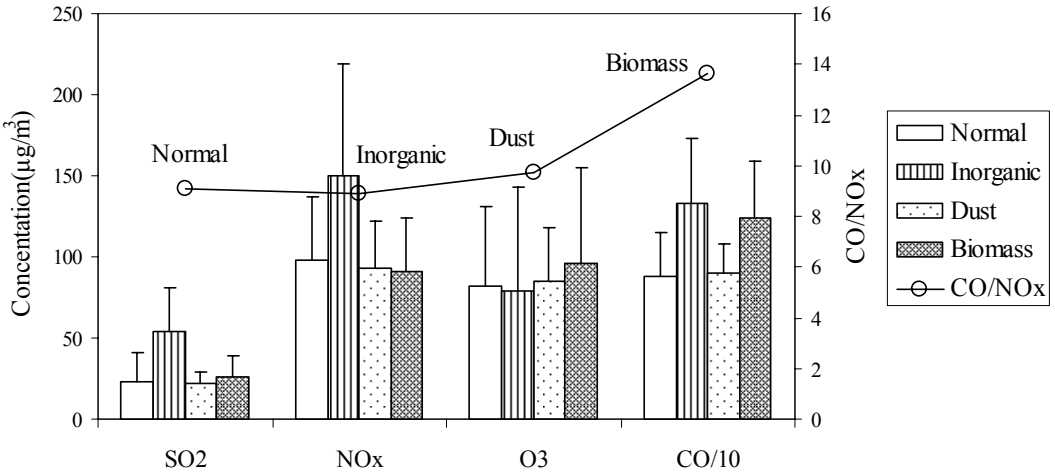

Fig. 10. The average concentrations of SO_2, NO_x, O_3 and CO during the normal period, PE1 (inogranic), PE2 (dust), and PE3 (biomass), respectively. The concentrations of CO were divided by 10 for scale visualization, and the ratios of CO/NO_x were also calculated and shown in the figure.

ACPD
11, 21713–21767, 2011

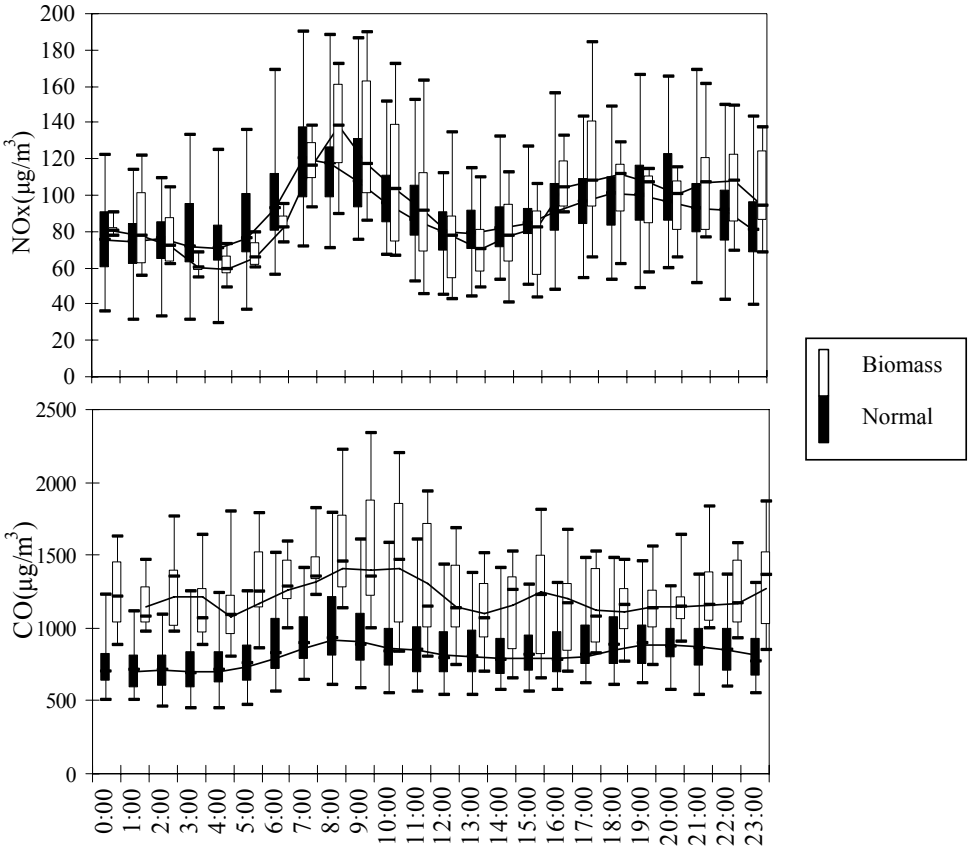

Fig. 11. The diurnal variation of CO and NO_x concentrations ($\mu g\,m^{-3}$) during the biomass burning period (white box) and normal period (black box), respectively. Horizontal lines represent the mean value; bottom and top of the boxes represent the 25 and 75 % limits, respectively; and bottom and top short lines represent the minimum and maxium values, respectively.

ACPD
11, 21713–21767, 2011

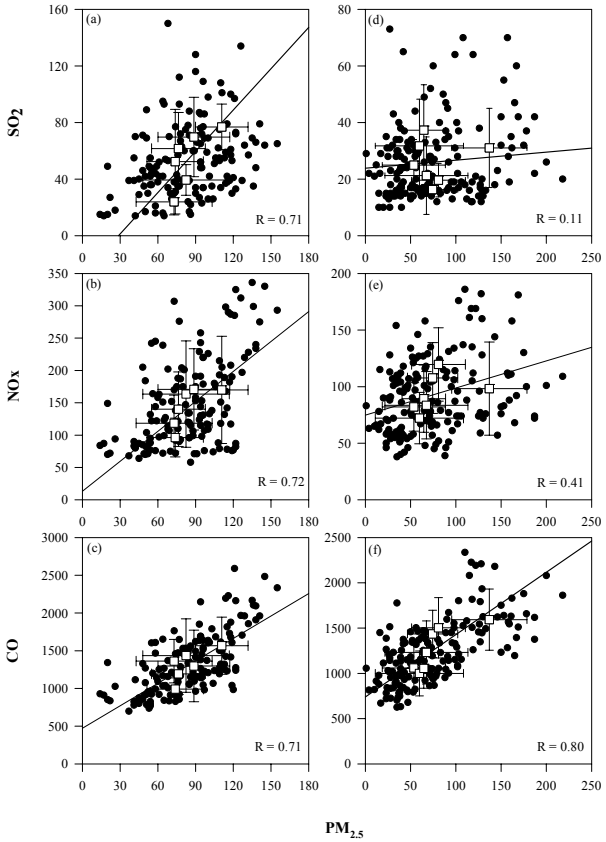

Fig. 12. The linear correlation between gaseous pollutants (SO_2, NO_x and CO) and $PM_{2.5}$, with correlation coefficients (R) shown in the figure. **(a–c)** denote PE1 and **(d–f)** denote PE3. The black dots denote the hourly data and the square symbols denote the daily average data, all units are in $\mu g\,m^{-3}$.

ACPD
11, 21713–21767, 2011